Cell Reports

Article

Actin Assembly around the *Shigella*-Containing Vacuole Promotes Successful Infection

Graphical Abstract

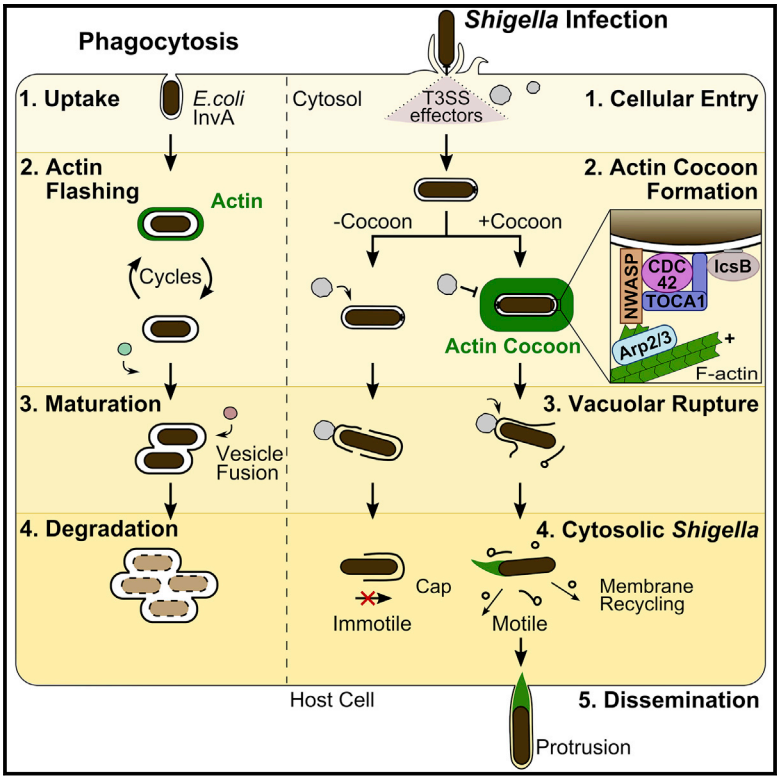

Highlights

- A thick actin cocoon forms *de novo* around the *Shigella*-containing vacuole upon entry
- The effector IcsB entraps host actin regulators at the vacuole by lipidation
- Cdc42, N-WASP, and the Arp2/3 complex are major actin cocoon regulators
- Cocoon formation promotes subsequent *Shigella* niche formation and dissemination

Authors

Sonja Kühn, John Bergqvist, Magdalena Gil, ..., Stéphanie Lebreton, Chiara Zurzolo, Jost Enninga

Correspondence

jost.enninga@pasteur.fr

In Brief

Kühn et al. present the formation of a massive actin cocoon structure around the *Shigella*-containing vacuole upon bacterial entry in enterocytes. This cocoon is formed by the pathogen-induced localization of host actin regulators at the phagosome. It favors efficient cytosolic access and spread for successful infection.

Kühn et al., 2020, Cell Reports *31*, 107638
May 12, 2020
https://doi.org/10.1016/j.celrep.2020.107638

CellPress

Cell Reports

CellPress
OPEN ACCESS

Article

Actin Assembly around the *Shigella*-Containing Vacuole Promotes Successful Infection

Sonja Kühn,[1,2] John Bergqvist,[1,2] Magdalena Gil,[1,2] Camila Valenzuela,[1,2] Laura Barrio,[1,2] Stéphanie Lebreton,[3] Chiara Zurzolo,[3] and Jost Enninga[1,2,4,*]

[1]Institut Pasteur, Department of Cell Biology and Infection, Dynamics of Host-Pathogen Interactions Unit, 25 Rue du Dr. Roux, 75015 Paris, France

[2]CNRS UMR3691, 25 Rue du Dr. Roux, 75015 Paris, France

[3]Institut Pasteur, Department of Cell Biology and Infection, Membrane Trafficking and Pathogenesis Unit, 28 Rue du Dr. Roux, 75015 Paris, France

[4]Lead Contact

*Correspondence: jost.enninga@pasteur.fr

https://doi.org/10.1016/j.celrep.2020.107638

SUMMARY

The enteroinvasive bacterium *Shigella flexneri* forces its uptake into non-phagocytic host cells through the translocation of T3SS effectors that subvert the actin cytoskeleton. Here, we report *de novo* actin polymerization after cellular entry around the bacterium-containing vacuole (BCV) leading to the formation of a dynamic actin cocoon. This cocoon is thicker than any described cellular actin structure and functions as a gatekeeper for the cytosolic access of the pathogen. Host CDC42, TOCA-1, N-WASP, WIP, the Arp2/3 complex, cortactin, coronin, and cofilin are recruited to the actin cocoon. They are subverted by T3SS effectors, such as IpgD, IpgB1, and IcsB. IcsB immobilizes components of the actin polymerization machinery at the BCV dependent on its fatty acyltransferase activity. This represents a unique microbial subversion strategy through localized entrapment of host actin regulators causing massive actin assembly. We propose that the cocoon promotes subsequent invasion steps for successful *Shigella* infection.

INTRODUCTION

Bacterial pathogens have evolved sophisticated ways to drive infection and to establish their intracellular niches for survival and replication. Especially the cellular actin cytoskeleton is extensively hijacked for bacterial purposes. This cytoskeletal meshwork is controlled by a complex network of actin-binding proteins (ABPs), which nucleate new actin filaments (F-actin) from actin monomers (G-actin) or elongate, maintain, and disassemble existing ones. ABPs are spatiotemporally localized and regulated by Rho GTPases, phospholipids, post-translational modifications, or membrane-bound scaffold (Le Clainche and Carlier, 2008; Rottner et al., 2017; Pollard, 2016). The main F-actin nucleating factor is the Arp2/3 complex (Machesky et al., 1994; Mullins et al., 1998), which generates branched actin meshworks in membrane ruffles and lamellipodia, at phagosomes and intracellular vesicles. Yet efficient F-actin nucleation requires additional nucleation-promoting factors (NPFs) such as N-WASP. N-WASP is itself activated by several factors, such as $PI(4,5)P_2$, the F-BAR scaffold TOCA-1, and the Rho GTPase CDC42 (Ho et al., 2004; Rohatgi et al., 1999; Rottner et al., 2017). Rho GTPases are central regulators of the actin cytoskeleton and switch between an inactive, GDP-bound and an active, GTP-bound state (Vetter and Wittinghofer, 2001). This is controlled by guanine nucleotide-exchange factors (GEFs) promoting GDP dissociation, GTPase-activating proteins (GAPs), and guanine nucleotide dissociation inhibitors (GDIs) (Etienne-Manneville and Hall, 2002; Cherfils and Zeghouf, 2013). In the active state, Rho GTPases interact with effector proteins for cell signaling and to regulate the actin cytoskeleton. Remarkably, bacterial pathogens such as the Gram-negative, enteroinvasive bacterium *Shigella flexneri* (hereafter *Shigella*) do not directly modify actin (Kühn and Mannherz, 2017). Instead, *Shigella* modulates the recruitment and the activation of actin regulators by subverting upstream Rho GTPases, kinases, and phospholipid signaling (Schnupf and Sansonetti, 2019; Schroeder and Hilbi, 2008; Valencia-Gallardo et al., 2015).

Shigella is the causative agent of bacterial dysentery and an important model for intracellular pathogenesis (Schnupf and Sansonetti, 2019). It forces its uptake into non-phagocytic epithelial cells through the translocation of type 3 secretion system (T3SS) effectors. These proteins target the host actin cytoskeleton and endomembrane trafficking to induce cellular entry and to establish an intracellular replicative niche. For cellular entry, thin membrane protrusions make the first contact with bacteria, followed by the initiation of massive actin rearrangements enclosing the entering *Shigella* (Schroeder and Hilbi, 2008; Valencia-Gallardo et al., 2015; Cossart and Sansonetti, 2004; Romero et al., 2012). After cellular uptake in a tight bacterium-containing vacuole (BCV) (Weiner et al., 2016), *Shigella* induces its rapid escape for replication into the host cytosol. There, it recruits the host actin nucleation machinery to one of its poles by

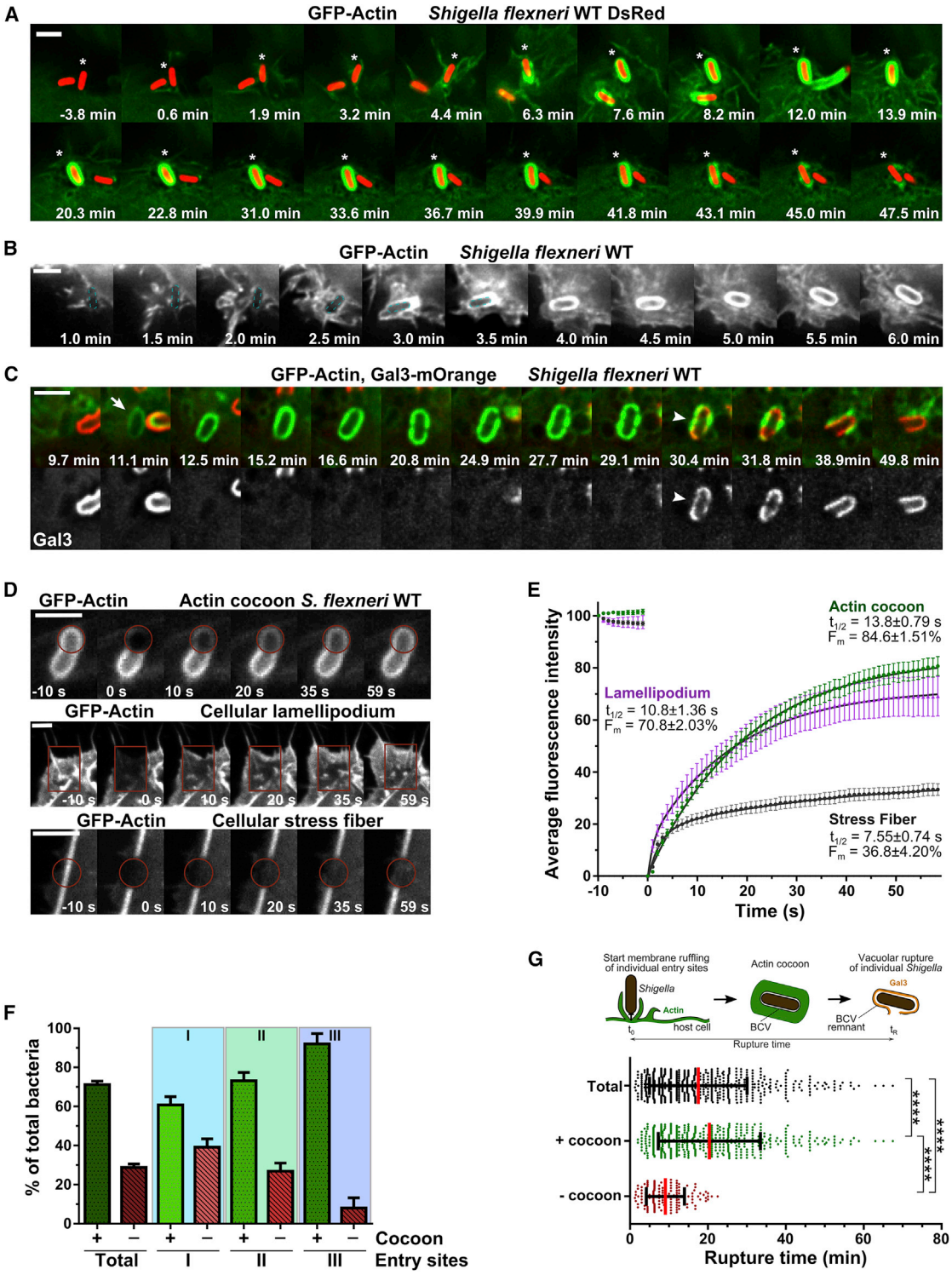

Figure 1. The Dynamic Actin Cocoon Polymerizes *De Novo* after Cellular Entry around *Shigella*'s BCV and Disassembles before Vacuolar Escape

(A and B) Real time-monitoring of the thick actin cocoon. HeLa cells expressing actin-GFP (green) were infected with *Shigella* WT DsRed (red) (A; asterisk denotes bacterium with cocoon) or *Shigella* WT (B; blue dashed line denotes bacterium). t = 0 min: onset of entry site formation.

(C) The actin cocoon needs to at least partially disassemble before vacuolar rupture. Time lapse of *Shigella* WT infecting HeLa cells expressing actin-GFP (green) and galectin-3-mOrange (red, Gal3). Arrow, newly formed cocoon; arrowhead, moment of rupture.

(legend continued on next page)

its virulence factor IcsA to spread from cell to cell (Suzuki et al., 1998; Egile et al., 1999; Gouin et al., 1999). Parallel to its uptake, *Shigella* induces the formation of infection-associated macropinosomes (IAMs). These IAMs accumulate at the entry site and surround the BCV. They form membrane-membrane contacts with the ruptured BCV, and their presence correlates with efficient rupture (Mellouk et al., 2014; Weiner et al., 2016).

We have recently discovered the formation of a hitherto undescribed actin cytoskeleton structure that assembles around vacuolar *Shigella* (Ehsani et al., 2012; Mellouk et al., 2014; Weiner et al., 2016). Here, we performed its in-depth characterization, coining it as an "actin cocoon." We found that this cocoon is thicker than any other cellular actin structure and assembles only after bacterial uptake. We identified the process underlying its formation, namely, the involved bacterial T3SS effectors and a subverted host pathway for actin rearrangements. Finally, we demonstrate that interfering with cocoon formation and disassembly affects *Shigella*'s capacity to invade the host cytosol.

RESULTS

The Actin Cocoon Assembles *In Situ* after Cellular Entry around *Shigella*-Containing Phagosomes, and Its Disassembly Precedes Cytosolic Escape

Actin-GFP transfected HeLa cells were imaged during early infection steps of wild-type (WT), dsRed-expressing *Shigella* at high spatiotemporal resolution (Figures 1A and 1B). After 2 h, almost all cells were infected, with no further primary infection, and membrane ruffling was shut down. Live imaging revealed the *in situ* assembly of a thick actin coat-like structure after pathogen entry, as indicated by a massive increase in fluorescence intensity around the BCV (Figures 1A and 1B; Videos S1 and S2). This structure, termed the "actin cocoon," was distinct from cortical actin and polymerized *de novo* at the surface of the entire vacuolar membrane. After a fast nucleation phase of 1–3 min, the actin cocoon was maintained until its final disassembly, which was immediately followed by BCV membrane rupture (Figures 1A–1C). All observed actin rearrangements took place in the time span after entry site formation and before the cytosolic spread of *Shigella*. Phalloidin staining of endogenous actin in fixed experiments revealed the presence of F-actin in the cocoon of *Shigella* invading HeLa or Caco-2 cells (Figures S1A and S1B).

To monitor the precise time point of vacuolar rupture in correlation to actin cocoon formation, we used fluorescently labeled galectin-3 as a marker. At the moment of vacuolar membrane damage, galectin-3 molecules are recruited to β-galactosides at the inner leaflet of the phagosomal membrane. We never observed vacuolar rupture by bacteria residing in an intact cocoon. At least a partial disassembly of the actin cocoon always preceded the directly following vacuolar rupture (Figure 1C). We conclude that cocoon disassembly is tightly linked with bacterial release into the host cytosol.

The Actin Cocoon Is Dynamically Re-assembled during Its Lifetime, and Its Formation Depends on the Time Point of Infection

Next, we performed fluorescence recovery after photobleaching (FRAP) measurements to compare the spatiotemporal dynamics of the actin cocoon with cellular stress fibers and the lamellipodium tip (Figures 1D and 1E). We anticipated fluorescence recovery either from F-actin treadmilling and *de novo* polymerization or to a lesser extent from free diffusion of cytoplasmic G-actin (a very fast saturated process). Strikingly, actin filaments of the cocoon had a high turnover rate, with a half-time of fluorescence recovery ($t_{1/2}$) of 13.8 ± 0.79 s and a mobile fraction (F_m) of 84.6% ± 1.51% (Figure 1D; Video S3). This revealed constant incorporation of new, unbleached G-actin and thus ongoing F-actin polymerization throughout the cocoon until its final disassembly. The same was observed by imaging with constant partial disassembly and re-assembly of the cocoon (Figure S1C). This points to constant *de novo* F-actin nucleation or elongation during its entire lifetime. We compared the cocoon with either very dynamic cellular actin structures, like the *de novo* assembling actin meshwork at lamellipodium tips, or very thick, like cellular stress fibers of F-actin bundles. We found the turnover of the cocoon to be similar to the lamellipodial tip ($t_{1/2}$ = 10.8 ± 1.36 s, F_m = 70.8% ± 2.03%) and clearly different compared with cellular stress fibers ($t_{1/2}$ = 7.55 ± 0.74 s, F_m = 36.8% ± 4.20%) (Figure 1E; Video S5).

To quantify *Shigella* infection with regard to actin cocoon formation and vacuolar rupture, we monitored the successive infection steps of individual bacteria (Figures S1D–S1G). Strikingly, in total 71.2% ± 1.75% of all *Shigella* assembled a dynamic actin cocoon before cytosolic escape (Figure 1F). *Shigella*'s probability for cocoon formation was pronounced in cells that had already been infected. This occurred with the same tendency, whether several bacteria entered via the same or via different entry sites (Figures 1F and S1G). We also quantified the time span that individual *Shigella* required after the start of entry site formation (initial cortical actin rearrangements) to escape into the host cytosol (initial galectin-3 recruitment). All bacteria invading at later time points polymerized an actin cocoon. This is shown by a significant delay in the rupture time point (−cocoon,

(D) Time lapses of FRAP experiments of the actin cocoon in comparison with cellular actin structures (see Videos S3, S4, and S5).
(E) Quantification of (D). Plotted are mean values ± 95% confidence interval [CI] and curve fit of at least 3 independent experiments (actin cocoon: n = 40 FRAP curves ; lamellipodial tip: n = 31; stress fibers: n = 75).
(F and G) Actin cocoon formation depends on the time point of bacterial infection and pre-infection. Depicted are percentages of bacteria that successfully escaped into the host cytosol and previously assembled an actin cocoon (+) or not (−) (F). On average, three entry sites formed per cell (Figures S1 and S2), and 71.2% ± 1.75% of invading bacteria (n = 631, 4 individual experiments) had a cocoon. All late invaders assembled a cocoon before vacuolar escape (G). Mean values ± SD of individual experiments (F) or rupture time points of pooled single invaders (G) are plotted. Mann-Whitney test with $p < 0.05$ as significant: ****$p < 0.0001$.
Scale bars: 3 μm. See Figures S1 and S2.

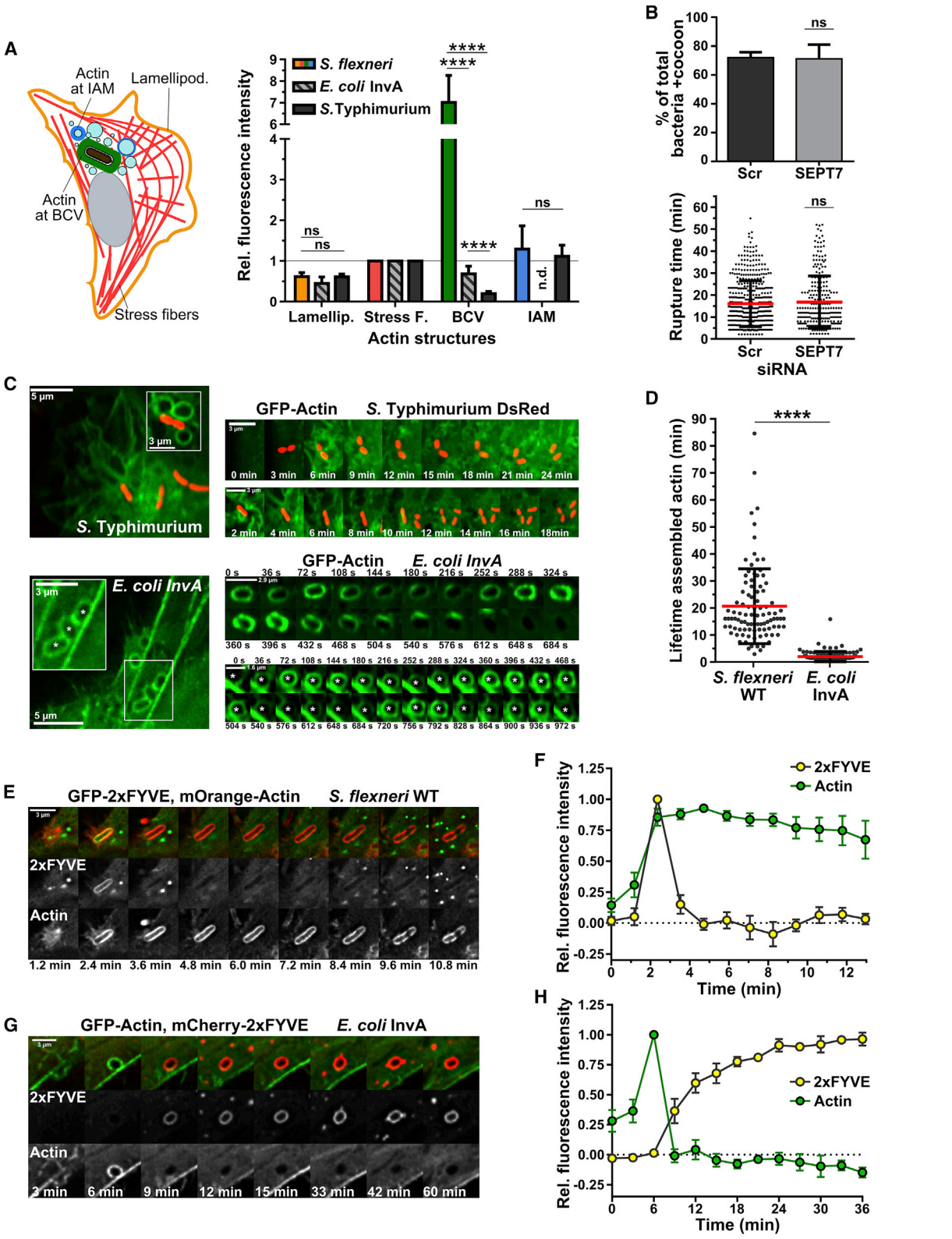

(legend on next page)

9.48 ± 5.63 min; +cocoon, 20.37 ± 13.13 min; $p < 0.0001$; Figure 1G). Increasing the multiplicity of infection (MOI > 15) increased the infection efficiency, with more bacteria invading via the same entry site, but not the probability of cocoon formation and rupture time (see Figure S2). Taken together, we conclude (1) that cocoon assembly depends on the phagocytic load as well as the order of infection and (2) that all late invading bacteria assemble an actin cocoon.

The *Shigella*-Specific Actin Cocoon Represents a Unique Structure

To better understand the nature of actin cocoons, we compared them with well-characterized host actin cytoskeletal structures in parallel to the FRAP experiments (Figure 2A). We measured the fluorescence intensities of the thickest stress fibers per infected cell and normalized each individual measurement against the average stress fiber intensity (see STAR Methods). Our analysis revealed that actin cocoons are much denser than any other actin structure, with on average 7-fold higher fluorescence intensity compared with stress fibers (7.02 ± 1.25, $p < 0.0001$) and 11.5-fold compared with the lamellipodium tip (0.61 ± 0.10, $p < 0.0001$) (Figure 2A). Remarkably, the actin turnover dynamics at the *Shigella* BCV result, although similar to the lamellipodium tip (Figure 1D), in a much thicker actin structure. In line with this, our previously published CLEM datasets of three actin cocoons (Weiner et al., 2016) exhibited a maximum thickness of 350 nm. Additionally, the cocoon differed from short-lasting actin rearrangements around *Shigella*-induced macropinosomes, which did not differ significantly in fluorescence intensity compared with stress fibers (1.30 ± 0.57; Figure 2A; Video S1), resembling the actin flashing phenomenon (Yam and Theriot, 2004; Liebl and Griffiths, 2009) (see below).

Next, we examined if other cytoskeletal systems, such as septin filaments (Kinoshita et al., 2002; Mavrakis et al., 2014), contribute to the assembly of this unique actin structure. During late infection steps, cytosolic *Shigella* are trapped in septin-actin cages that restrict bacterial proliferation (Mostowy and Cossart, 2012; Mostowy et al., 2010, 2011). We performed knockdown of SEPT7 by RNA interference, a common technique for the efficient inhibition of septin filament formation (Sirianni et al., 2016). This neither prevented cocoon formation nor delayed *Shigella*'s cytosolic escape (Figure 2B; Figures S3A, S3B, and S3F). Therefore, the actin cocoon around vacuolar *Shigella* forms independently of septin 7.

Furthermore, we deciphered if the actin cocoon is specific for *Shigella* or a general mechanism occurring during cell entry. Therefore, we compared it with actin rearrangements during early infections of the closely related bacterium *Salmonella enterica* serovar Typhimurium (*S.* Typhimurium). Like *Shigella*, *Salmonellae* induce massive membrane ruffling and macropinocytosis during cellular entry by T3SS effector proteins. To the contrary, *S.* Typhimurium pursue mainly an intravacuolar lifestyle for bacterial replication (Santos and Enninga, 2016). To decipher actin polymerization around entering *Salmonella*, we followed bacteria-induced actin rearrangements during the first 2 h of infection (Figures 2A and 2C). We barely detected any around *Salmonella*-containing vacuoles (SCVs) (35-fold fewer, 0.20 ± 0.05) (Figures 2A and 2C). Instead, actin occurred as small, intense dots around the SCV, probably derived from recycling and fusion events for vacuolar maturation. We concluded that *Salmonella* does not assemble an actin coat-like structure during early invasion steps.

Finally, we examined the host cell contribution for cocoon assembly. Previous work of several groups described short-lasting, repeated cycles of actin polymerization and depolymerization around fully internalized phagosomes. These actin rearrangements, termed "actin flashing," were identified as downstream consequences of several cellular entry mechanisms independent of cell type and cargo in cells with high phagocytic load (Yam and Theriot, 2004; Liebl and Griffiths, 2009). To compare actin flashes with actin cocoons, we infected HeLa cells with *Escherichia coli*-expressing *Yersinia pseudotuberculosis* invasin A (*E. coli* InvA) as model for canonical phagocytosis. Invasin A binds integrins and is sufficient to transfer *Yersinia*'s zippering entry to *E. coli* (Isberg et al., 1987). We observed successive waves of actin flashing around internalized *E. coli* InvA with 32% lower fluorescence intensity compared with stress fibers (0.68 ± 0.19, $p = 0.0056$). In line with previous studies (Yam and Theriot, 2004; Liebl and Griffiths, 2009), the duration was 2.0 ± 1.9 min per cycle (Figures 2A, 2C, and 2D). Thus, actin cocoons were distinct from the "actin flashing" phenomenon in several major points. First, the fluorescence intensity of *Shigella*'s cocoons was on average 10-fold higher (Figure 2A). Second, the cocoon had a 10 times longer lifespan than one

Figure 2. The Actin Cocoon Is a *Shigella*-Specific Cytoskeletal Structure

(A) The actin cocoon is thicker than any cellular actin structure and is *Shigella* specific. Left: scheme of investigated actin structures with stress fibers (Stress F.; red), lamellipodial tip (Lamellip; orange), and actin at BCVs (bacterium-containing vacuole; green) and at IAMs (infection-associated macropinosome; blue). Right: quantification of relative fluorescence intensities of actin-GFP (*S. flexneri* WT: n = 250; *E. coli* InvA: n = 236; *S.* Typhimurium WT: n = 322).

(B) The actin cocoon assembles independently of septin 7 after siRNA-mediated knockdown (KD) (Scr: scramble, control, n = 264 cytosolic bacteria; SEPT7, n = 250; KD 91.7%; see Figure S3).

(C) Time-lapse imaging examples of (A). Top: invading *S.* Typhimurium did not assemble an actin cocoon. Bottom: cyclic actin flashing around *E. coli* InvA phagosomes (asterisk) in comparison with cellular stress fibers.

(D) The actin cocoon lifetime of *Shigella* WT (20.64 ± 13.87 min; n = 95) differs from actin flashing by *E. coli* InvA (n = 103).

(E and G) Representative time lapses of HeLa cells co-transfected with the PI3P marker 2xFYVE and actin and infected either with *Shigella* WT (E) or *E. coli* InvA (G).

(F and H) Quantification of (E) and (G) with cytosolic background correction and normalized to the maximal fluorescence intensity (*S. flexneri* WT: n = 12; *E. coli* InvA: n = 12; mean values ± SEM).

Statistical significance: Student's t test with $p < 0.05$ as significant: ****$p < 0.0001$; ns, not significant. Indicated are mean values ± SD of at least 3 independent experiments. See Figures S3 and S4.

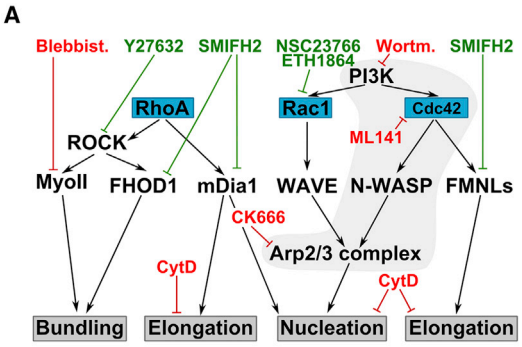

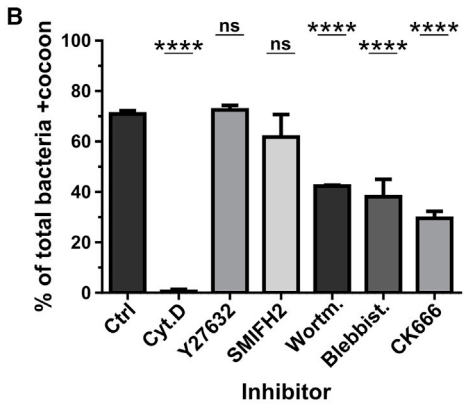

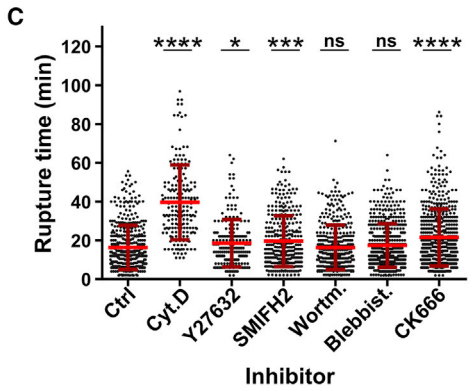

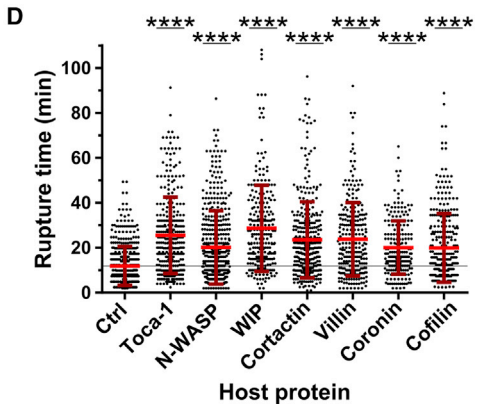

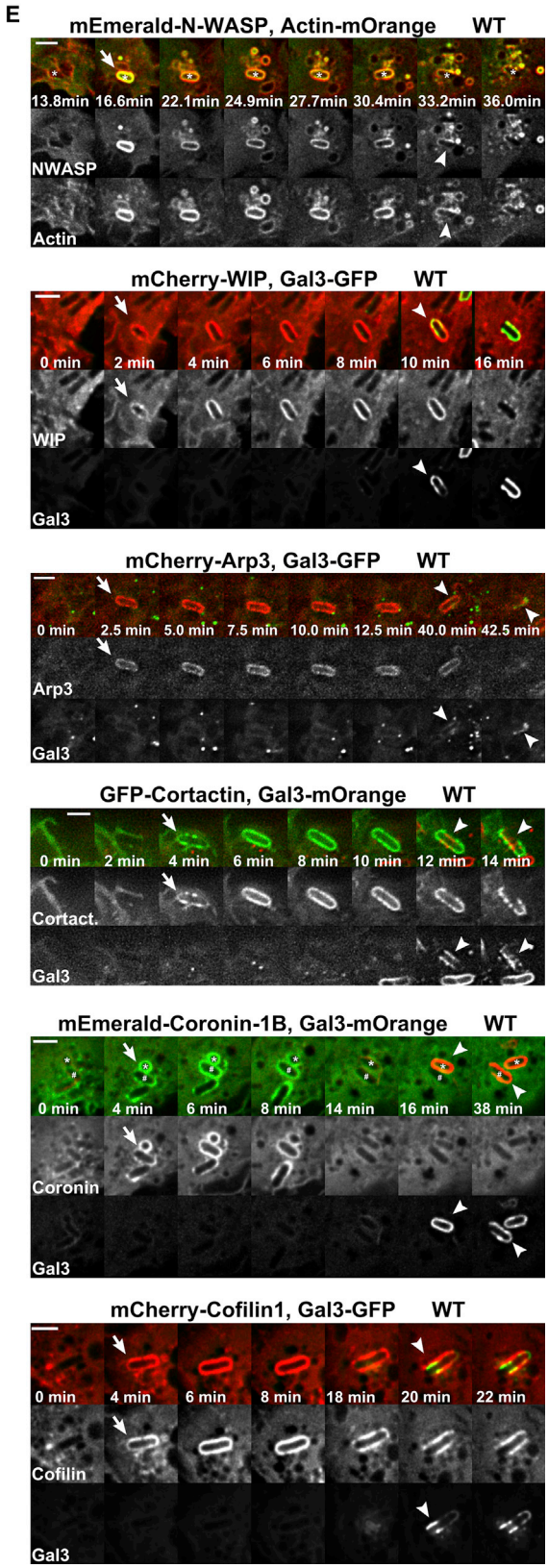

(legend on next page)

actin flash (Figure 2D). Third, we did not identify any consecutive cycles of actin assembly at *Shigella*'s BCV. Cocoon disassembly was always followed by immediate cytosolic escape, while *E. coli* InvA phagosomes never ruptured. In conclusion, the actin cocoon around vacuolar *Shigella* clearly differs from transient actin structures around endocytic compartments.

Actin Cocoon Assembly Precedes Diversion from Canonical Phagosomal Maturation

To obtain more details about *Shigella*'s vacuolar identity, we investigated the recruitment of markers for canonical phagosome maturation and autophagy to the BCV. We previously realized an altered lipid and protein composition of the two compartments induced during *Shigella* infection. Although canonical maturation and recycling of IAMs is followed through PI3P, Rab5, Rab7, and Rab11 recruitment (Mellouk et al., 2014; Weiner et al., 2016; Kühn et al., 2017), PI3P was only very transiently detected at the *Shigella* BCV (Weiner et al., 2016). Remarkably, the actin cocoon forms at the onset of this short lifetime PI3P peak (Figures 2E and 2F). Although PI3P is quickly and irreversible depleted from the BCV, the cocoon remains assembled (Figures 2E and 2F). Cocoon disassembly is followed by immediate vacuolar rupture without the BCV's becoming PI3P positive again or recruiting Rab7 (Figure 2E; Figure S4A). In contrast, depletion of the thin actin coat around the canonical phagosomes of *E. coli* InvA, like the last actin flashing peak, was proceeded by a long PI3P peak (Figures 2G and 2H). This is followed by Rab7 enrichment at the *E. coli* InvA phagosome and PI3P depletion (Figure S4B), indicating phagosomal maturation by vesicle fusion events favoring degradative pathways. In addition, LAMP1 and LC3 are also not recruited to the *Shigella* BCV or the actin cocoon (Figures S4C and S4D). In conclusion, actin cocoon assembly correlates with the moment when the *Shigella* vacuole changes its identity, with no Rab7 recruitment and the avoidance of the late endocytic pathway, eventually leading to bacterial degradation (Figure S4E).

The Host Arp2/3 Complex-Dependent Actin Nucleation Machinery Is Recruited to the BCV

In order to identify host factors that initiate actin cocoon formation, we performed an inhibitor screen targeting host actin regulators (Figure 3A). A general complication in examining intracellular, pathogen-induced actin cytoskeleton subversions is that the studied events are downstream of cellular entry. Manipulation will, necessarily, also interfere with invasion efficiency. To overcome this, we used conditions that still enabled pathogen entry and had a measurable effect on cocoon formation (see STAR Methods). Furthermore, we focused only on *Shigella* that successfully invaded the host cytosol (galectin-3-positive BCV) as an indicator of efficient infection. The readout rupture time can indicate changes in actin cocoon dynamics but is not sufficient, because it includes successive actin-regulated steps from cellular uptake to vacuolar rupture (Figure S1D). For this reason, we analyzed in parallel the percentage of bacteria per cell with actin cocoon (Figure 3B). We observed the strongest impact by the inhibition of the Arp2/3 complex with a 2.5-fold reduction of actin cocoons per cell (+CK666, 29.6% ± 2.76%; $p < 0.0001$). Although Arp2/3 complex inhibition did not impede bacterial uptake, it was sufficient to prevent F-actin nucleation at the BCV (Figure 3B). Thus, the Arp2/3 complex regulates cocoon assembly. Interestingly, inhibition of PI3 kinases (42.3% ± 0.41%, $p < 0.0001$) or myosin II (38.1% ± 6.92%, $p < 0.0001$) significantly reduced the amount of actin cocoons (Figure 3B), and the remaining ones had decreased thickness and a less dense F-actin meshwork, respectively. On the other hand, inhibition of formins or ROCK kinase did not prevent cocoon formation (Figure 3B). Yet *Shigella* entered delayed into formin-inhibited cells (19.6 ± 13.1 min, $p = 0.0007$; Figure 3C). Eventually, formins might be rather involved in cocoon maintenance by F-actin elongation than filament nucleation. After inhibition of actin polymerization by cytochalasin D, we barely detected actin rearrangements at the entry site and no cocoon-like structure (Figure 3B), underlining again that cocoon assembly requires *de novo* F-actin polymerization. We also observed a strongly reduced infection rate, probably caused by impaired actin rearrangements at the entry site and in line with the increased vacuolar rupture time (+DMSO, 16.4 ± 11.4 min; +CytD, 39.6 ± 19.3 min; $p < 0.0001$). Taken together, these results emphasize first a role of Arp2/3-mediated actin rearrangements around the vacuolar niche of *Shigella*. Second, preventing or perturbing actin cocoon formation at *Shigella*'s BCV affects cytosolic access, underlining the importance of the cocoon for intracellular niche formation.

To identify host factors involved in actin cocoon formation, we overexpressed selected ABPs and their regulators. We hypothesized that their cellular excess interferes with F-actin polymerization and, in case these proteins are involved in cocoon regulation, potentially alters *Shigella*'s cytosolic access. We first screened ABPs for their recruitment to infection sites,

Figure 3. Host Actin Regulators Are Involved in Actin Cocoon Assembly and Are Recruited to *Shigella*'s BCV before Vacuolar Escape

(A) Scheme of host proteins inhibited by compounds of the inhibitor screen (B and C; see also Figures 4F, S5F, S6C, and S6D). Blue box, Rho GTPases; black, ABPs and their regulators; gray box, effect on F-actin; red, inhibits cocoon assembly; green, no effect on initial cocoon assembly. CytD, cytochalasin D, an actin polymerization inhibitor; SMIFH2, formin inhibitor; Y27632, ROCK inhibitor; Blebbist, blebbistatin, a myosin II inhibitor; Wortm, wortmannin, a PI3K inhibitor; CK666, Arp2/3 inhibitor; NSC23766, RAC1 GEF inhibitor; ETH1864, RAC1 inhibitor; ML141, CDC42 inhibitor.

(B and C) Quantitative analysis of inhibitor screens identifies host proteins and signaling pathways involved in cocoon assembly (B) and cytosolic access (C) (n = 2,912 total invaders, on average 416 per condition; Ctrl, DMSO control).

(D) Overexpression of seven selected host ABPs that interfere with the timing of vacuolar rupture with galectin-3-mOrange (Ctrl, control; n = 2,641, on average 330 per condition).

(E) Recruitment of host ABPs to *Shigella*'s BCV before cytosolic escape. Time lapses of HeLa cells expressing fluorescently tagged host proteins and actin or galectin-3 (Gal3; scale bars: 3 μm). Arrow, recruitment to BCV; arrowhead, vacuolar rupture.

Indicated are mean values ± SD of at least 3 independent experiments. Student's t test with $p < 0.05$ as significant compared with controls: *$p < 0.05$, ***$p < 0.001$, and ****$p < 0.0001$; ns, not significant.

determined afterward the rupture time of positive candidates, and finally monitored their precise subcellular localization (Figures 3D and 3E). Remarkably, cytosolic escape of *Shigella* invading cells overexpressing TOCA-1 (also known as FNBP1L), N-WASP, WIP, cortactin, villin, coronin-1B, or cofilin-1 was significantly delayed (Figure 3D). N-WASP is an NPF for the Arp2/3 complex stabilized by WIP and activated by CDC42-GTP, TOCA-1, and $PI(4,5)P_2$. TOCA-1 activity itself is regulated by CDC42 and $PI(4,5)P_2$ (Rottner et al., 2017; Ho et al., 2004; Rohatgi et al., 1999). Cortactin binds to F-actin and the Arp2/3 complex and links signaling, cytoskeleton, as well as trafficking proteins to actin filaments (Kirkbride et al., 2011). Overexpression of these ABPs probably caused increased F-actin nucleation at the BCV membrane. Villin bundles F-actin, and its overexpression likely stabilizes actin cocoons. Furthermore, coronin-1B collaborates with cofilin-1 in actin disassembly (Cai et al., 2008; Chan et al., 2011). Overexpression of actin, coronin-1B, or cofilin-1 may boost F-actin turnover and polymerization at *Shigella*'s BCV. Because cocoons exhibited clear borders with uniformly distributed, exceptionally high fluorescence intensity (Figures 1A–1C), and because of the identified ABPs (Figure 3), we expect a rather stiff, highly bundled, and cross-linked F-actin meshwork.

Next, we performed time-lapse microscopy of *Shigella* infections in cells co-transfected with the involved host proteins and galectin-3. We followed their recruitment to the BCV and correlated their localization with the time point of cytosolic escape (Figure 3E). N-WASP was recruited to the *Shigella*-containing vacuole and co-localized there with actin. We did not observe any case of N-WASP recruitment to the BCV without actin assembly or vice versa. In addition, WIP, the Arp2/3 complex component Arp3, and cortactin were recruited to the BCV membrane and all were, like actin (Figure 1C), at least partially depleted before vacuolar rupture (Figure 3E). Coronin-1B was recruited early during infection and cocoon assembly, while cofilin-1 localized around the vacuolar membrane remnant even after rupture (Figure 3E). Taken together, we identified a network of host actin regulators that are recruited to *Shigella*'s BCV and regulate cytosolic invasion.

Actin Cocoon Formation Depends on CDC42-Activated and Arp2/3 Complex-Mediated F-Actin Nucleation

We next identified the involved upstream Rho GTPase signaling for Arp2/3 complex-mediated actin cocoon assembly combining RNA interference, inhibitors, and loss-of-function mutations. Knockdown of CDC42 and the Arp2/3 complex component ArpC3 resulted in clearly altered entry sites compared with the control (Figures 4A–4C). Although CDC42 knockdown or overexpression of its inactive mutant strongly reduces infection efficiency up to 75% (Mounier et al., 1999; Mellouk et al., 2014), it does not entirely prevent cellular uptake in our experiments (Figures 4B–4D; Figures S5A–S5E). Hence, we considered only bacteria that successfully invaded host cells to focus on the role of the actin cocoon. Strikingly, cocoon formation was completely or strongly abolished by knockdown of CDC42 and ArpC3, respectively (+siRNA [small interfering RNA] CDC42, 2.60% ± 1.84%; +siRNA ArpC3, 16.6% ± 0.47%; Figure 4D). We confirmed the strong delay of *Shigella* vacuolar rupture in CDC42- and ArpC3-depleted cells (Figures S5D and S5E) (Mellouk et al., 2014). Similar results were obtained in cells treated with the CDC42 inhibitor ML141 (Figure S5F). Interestingly, although knockdown of ARPC3 was very efficient, cocoon formation was not as strongly inhibited as for CDC42 (Figure 4D). Either the remaining amount of Arp2/3 complex was sufficient to assemble some cocoons, or another, CDC42-dependent actin polymerization pathway might be involved, for example, via formins. In addition, we investigated the dependence of CDC42 activity on vacuolar escape by comparing the vacuolar rupture time of invading *Shigella* in cells overexpressing CDC42 WT, a GDP- or GTP-bound CDC42 mutant. Locking CDC42 in either an active or inactive state significantly delayed the cytosolic escape of *Shigella* (Figure 4E; Figures S5G–S5J). Thus, cytosolic release of *Shigella* strongly depends on the ability of CDC42 to function as a molecular switch. Finally, RAC1 is probably not essential for *de novo* actin cocoon assembly, as we did not observe a significant effect in cocoon assembly and cytosolic escape by its knockdown or inhibition with ETH1864 and NSC23766 (Figure 4F; Figures S6A–S6D). Consequently, cocoon assembly requires CDC42-activated and Arp2/3 complex-mediated F-actin nucleation with CDC42 signaling via N-WASP. Thus, the main NPF of the Arp2/3 complex at the BCV is N-WASP.

Actin Cocoon Assembly Is Regulated by *Shigella* T3SS Effector Proteins

To identify which *Shigella* effectors are involved in actin cocoon regulation, we screened a *Shigella* mutant library with single T3SS effector deletions (Sidik et al., 2014). Results of nine selected mutants are presented (Figures 5A and 5B). As the amount of entering bacteria per cell varies for different mutants, we focused our analysis on the first invading bacteria of individual strains. Strikingly, single deletions of the bacterial effectors IpgD, IpgB1, and IcsB strongly increased cytoskeletal rearrangements around the BCV. We found up to threefold more Δ*icsB* residing in an actin-containing structure before cytosolic escape (Figure 5A; Figure S6E). We could also confirm our previous reported finding that IpgD increases cocoon formation of the total invading population (Mellouk et al., 2014). The rupture timing of Δ*ipgB1*, Δ*virA*, and Δ*icsB* was likewise significantly delayed (Figure 5B). IcsA recruits N-WASP to the pole of cytosolic bacteria for actin tail formation (Suzuki et al., 1998; Egile et al., 1999) but is not accessible before vacuolar rupture. Consistent with this, we observed no effect on cocoon assembly in Δ*icsA* infections (Figure 5A). Thus, IpgD, IpgB1, and IcsB play a role in actin cocoon regulation. Deletion of these *Shigella* effectors might lead to a misregulation of the cocoon with a disturbed actin turnover.

Clustering of Host Actin Regulators at *Shigella*'s BCV Depends on the Fatty Acyltransferase Activity of the T3SS Effector IcsB

We next questioned if the recruitment of the actin nucleation machinery at the BCV (Figure 3E) depends on specific *Shigella* effectors. We focused on IcsB, the strongest hit of our T3SS effector screen (Figures 5A and 5B). During canonical phagocytosis, active CDC42 localizes to forming pseudopods but is

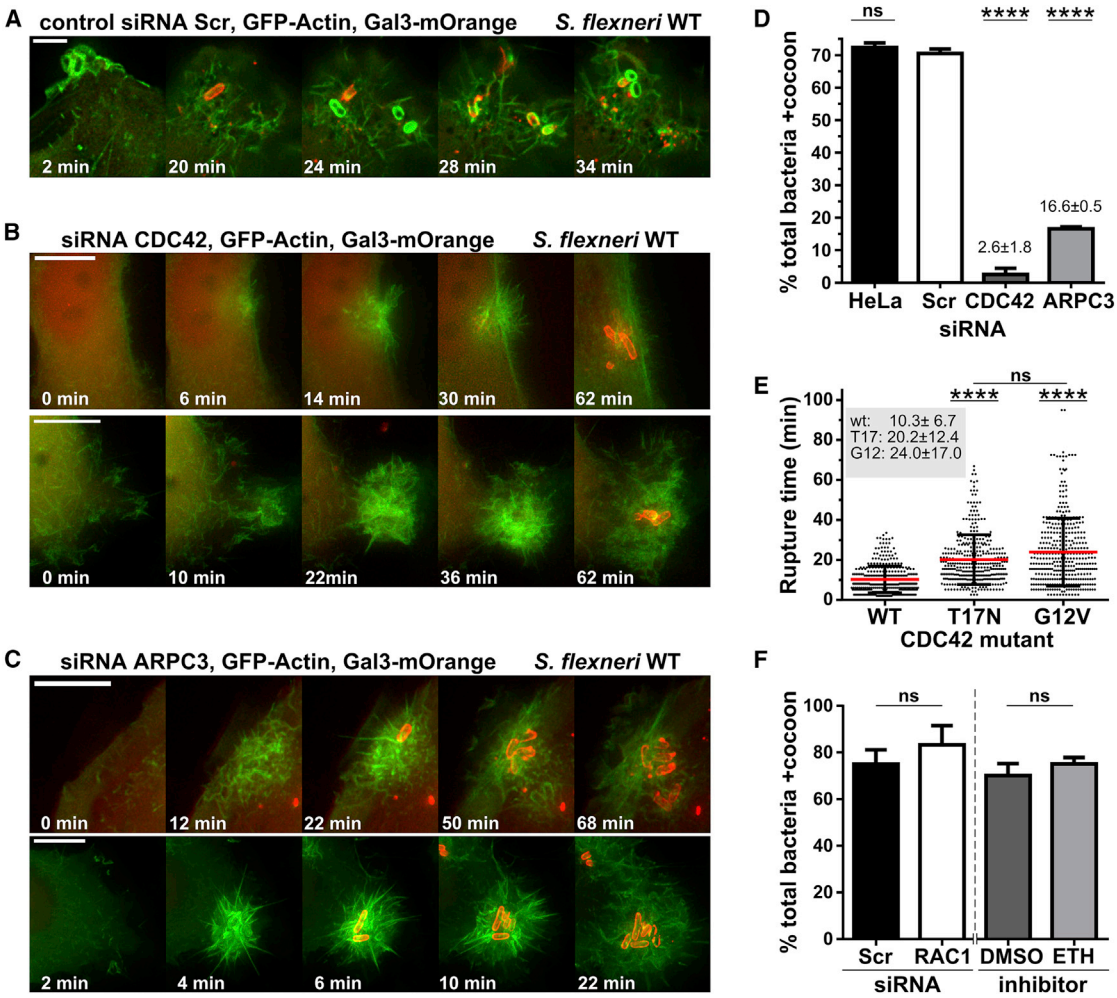

Figure 4. CDC42-Activated F-Actin Nucleation by the Arp2/3 Complex Is Essential for Cocoon Formation

(A–D) Knockdown of CDC42 or the Arp2/3 complex subunit ARPC3 inhibits cocoon assembly. Representative time lapses monitoring actin rearrangements during early *Shigella* WT infection are presented for the scramble siRNA-treated control (Scr; A), for CDC42 (B; KD 87.1%), and for ARPC3 knockdown (C; KD 95.6%) (scales: 5 μm, 1.05 μm z stack; see Figure S3F). (D) Quantitative analysis of actin cocoon assembly shows strongly reduced cocoon formation (no siRNA [HeLa], n = 374 bacteria; siRNA Scr, n = 481; siRNA CDC42, n = 464; siRNA ARPC3, n = 573).

(E) The ability of CDC42 to cycle between an active and inactive state is required for efficient cytosolic access of *Shigella*. T17N, inactive, GDP-bound mutant; G12V, active, GTP-bound mutant (n = 1,123 total rupture events; WT, n = 373; T17N, n = 375; G12V, n = 375).

(F) Neither RNAi-mediated RAC1 knockdown nor its inhibition by the RAC1 inhibitor ETH1864 alters actin cocoon assembly (siRNA Scr, n = 386; siRNA RAC1, n = 409; DMSO, n = 385; ETH1864, n = 328).

Depicted are mean values ± SD of 3 independent experiments; $p < 0.05$ is significant compared with control: ****$p < 0.0001$; ns, not significant. See Figures 3A, S3, S5, and S6.

inactivated and depleted to complete cup closure (Niedergang and Grinstein, 2018; Freeman and Grinstein, 2014; Hoppe and Swanson, 2004). Likewise, CDC42 initiates *de novo* F-actin rearrangements for *Shigella*'s cellular uptake (Adam et al., 1996). We confirmed CDC42 recruitment to forming membrane ruffles during *Shigella* infection. Yet contrary to canonical phagocytosis, CDC42 remained at the BCV after cellular uptake and persisted with galectin-3 at the membrane remnant (91.9% ± 1.56% of cytosolic bacteria; Figures 5C and 5D). Remarkably, we deciphered that this constant localization of CDC42 depends on IcsB (Figure 5E). We followed the successive invasion steps of individual bacteria and quantified the recruitment of CDC42 to their BCV as well as the BCV membrane remnant at the moment of vacuolar rupture. Deletion of IcsB did not interfere with initial CDC42 recruitment to membrane ruffles but led to its depletion from the BCV before vacuolar rupture (Figure 5F). Although the Rho GTPase RAC1 is likewise clustered at the BCV dependent on IcsB (Figures S7A and S7B), it is not essential for cocoon assembly (Figures 4F and S6A–S6D). We detected only a few cases of RhoA recruitment (Figure S7C). As for CDC42, TOCA-1 also constantly localized IcsB dependent at *Shigella*'s vacuole following initial recruitment (Figure 5G). Noteworthy, although

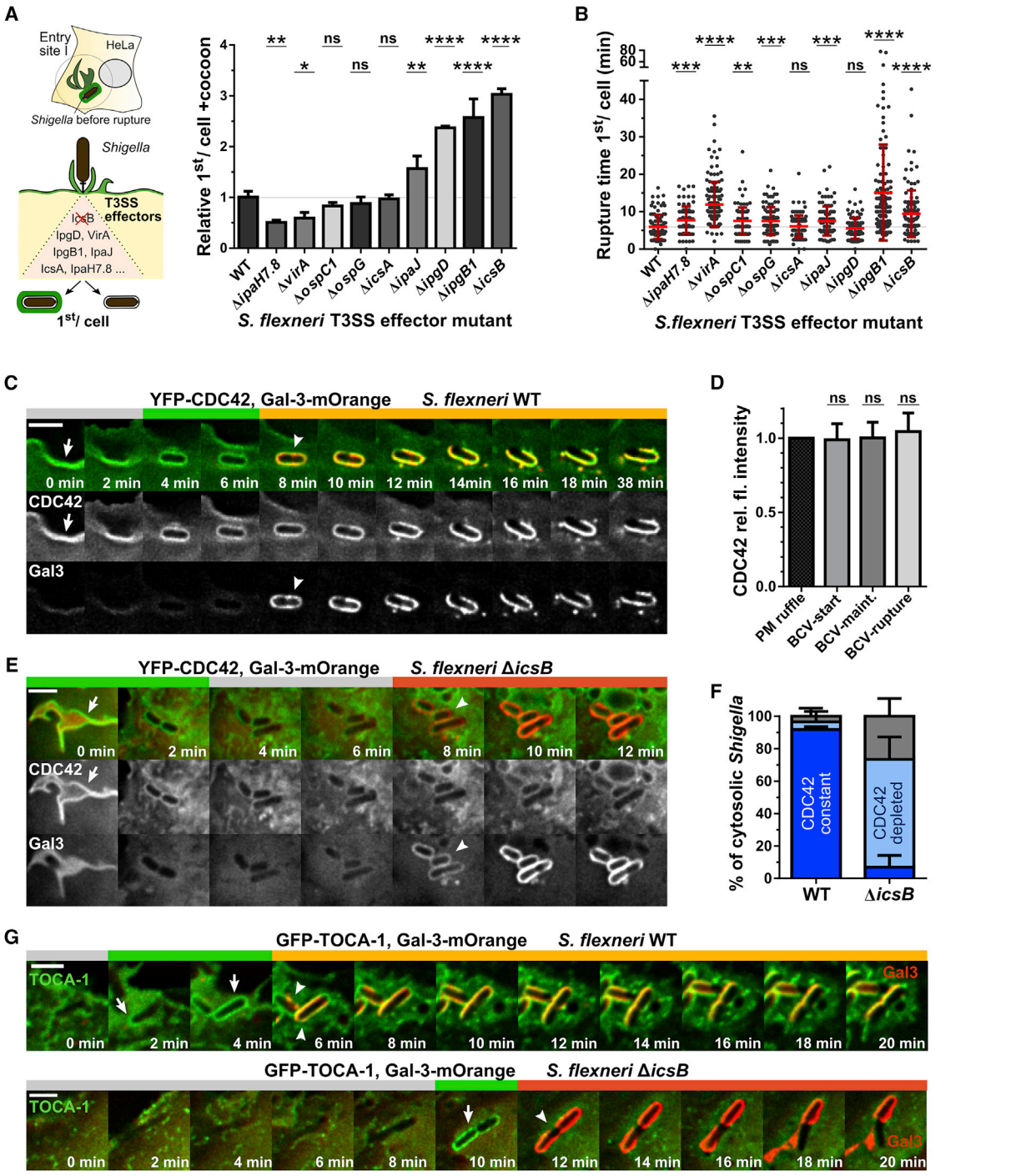

Figure 5. The Actin Cocoon Is Regulated by *Shigella* T3SS Effector Proteins, and Host Actin Regulators Constantly Localize IcsB Dependent at the BCV

(A and B) Infection of HeLa cells expressing actin-GFP and galectin-3-mOrange by *Shigella* single effector deletion mutants. The first invading bacteria per cell was analyzed with regard to actin cocoon assembly (A) and rupture time (B). (n = 1,085 total counted bacteria; WT, n = 101; Δ*ipaH7.8*, n = 80; Δ*virA*, n = 131; Δ*ospC1*, n = 112; Δ*icsA*, n = 103; Δ*ipaJ*, n = 95; Δ*ipgD*, n = 121; Δ*ipgB1*, n = 116; Δ*icsB*, n = 120. $p < 0.05$ is significant compared with WT: *$p < 0.05$, **$p < 0.01$, ***$p < 0.001$, and ****$p < 0.0001$; ns, not significant).

(C) Representative time lapses of constant CDC42 localization at the BCV during *Shigella* WT infection.

(D) Quantification of the normalized relative fluorescence intensity of CDC42 recruitment during successive *Shigella* invasion steps. PM ruffle, fluorescence intensity at plasma membrane ruffles; BCV-start, at the phagocytic cup before scission; BCV-maint, at maintained BCV after cellular uptake; BCV-rupture, at BCV after rupture.

(legend continued on next page)

the membrane remnant was quickly recycled in WT *Shigella* infections, it remained loosely and sticky around cytosolic Δ*icsB* bacteria (Figures 6E–6G).

Furthermore, we found N-WASP to constantly localize around *Shigella*'s endocytic compartment in HeLa and Caco-2 cells (Figures 6A and S7D). N-WASP was recruited after cellular entry to 78.6% ± 3.25% of WT bacteria that successfully escaped from the BCV and remained associated with the BCV membrane remnants in 69.2% ± 9.45% of the cases (Figures 6A and 6D). As for CDC42, the permanent localization of N-WASP at the BCV, but not its initial recruitment, was IcsB dependent (Figures 6B and 6D). We further confirmed N-WASP recruitment to be independent of the *Shigella* virulence factor IcsA (Figure S7E). We hypothesized that CDC42 initiates N-WASP recruitment, as CDC42 localizes during early entry steps at membrane ruffles. Therefore, we knocked down CDC42 and followed the localization of N-WASP during *Shigella* WT infection (Figure 6C). Interestingly, we found a strong reduction in initial N-WASP recruitment to the BCV (16.67% ± 7.92%), but recruited N-WASP remained localized (14.48% ± 4.84%) (Figure 6D). Residual CDC42 activity was probably sufficient to recruit N-WASP in some rare cases with constant BCV localization because of IcsB.

It has recently been discovered that IcsB post-translationally modifies the actin regulators identified herein by 18-carbon lipidation (Liu et al., 2018). IcsB is an acyltransferase, which catalyzes N^{ε}-fatty acylation of lysine residues in membrane-bound host proteins (Liu et al., 2018). A C306A-IcsB mutant has been described to be crucial for IcsB activity (Liu et al., 2018). Therefore, we analyzed the role of the IcsB enzymatic activity during cocoon formation. Although complementation of the *icsB*$^{-}$ mutant with IcsB resembled the phenotype of *Shigella* WT infections, expression of the acyltransferase-inactive IcsB-C306A mutant (*icsB*$^{-}$ [C306A]) impaired N-WASP clustering at the *Shigella* vacuole (Figures 6F and 6G; Figures S7F–S7H). Thus, we found that IcsB clusters key factors of the host actin nucleation machinery at the BCV dependent on its fatty acyltransferase enzymatic activity. However, the initial recruitment of the Arp2/3 complex activator N-WASP depends on CDC42 signaling. Because knockdown of CDC42 prevents cocoon formation, the CDC42-mediated activation of N-WASP is crucial for actin cocoon assembly.

Function of the Actin Cocoon in Late Intracellular Infection Steps

We finally deciphered the consequences of actin cocoon assembly on subsequent infection steps following cytosolic release of *Shigella* from the vacuole. Here, we monitored the successive invasion events for each individual bacterium from cell entry to protrusion for cell-to-cell spread and quantified the fate of the bacterium and its BCV remnant 2 h post-infection (Figures 7A–7D). Here, 78.7% ± 9.40% of the bacteria that assembled an actin cocoon prior to vacuolar rupture were motile (Figure 7B). In contrast, *Shigella* without cocoon had a high probability of being trapped inside the cytosol either by not starting or by stopped actin tail-mediated movement (62.3% ± 0.24%; Figure 7B). In addition, the majority of *Shigella* with a cocoon were BCV membrane remnant free (Figure 7C). Bacteria without a cocoon showed difficulties in unwrapping the BCV membrane remnants and were predominantly surrounded by a part of it (68.6% ± 3.91%; Figure 7C). Such remnants or "membrane caps" impaired *Shigella* spreading, as 69.7% ± 11.8% of them were unable to move at the end of the experiments. In contrast, actin cocoon-supported loss of the BCV membrane fostered successful spreading (73.8% ± 4.03% motile after sticky removal, 100% motile after quick recycling; Figure 7D). Taken together, the actin cocoon supports late cell invasion steps and cell-to-cell spread by aiding to the removal of the BCV membrane remnant, which impairs *Shigella*'s motility.

DISCUSSION

We identified in this study highly dynamic *de novo* F-actin polymerization of exceptional thickness around the endocytic vacuole of intracellular *Shigella*. We showed that this actin cocoon assembles after scission at the surface of the entire vacuolar membrane and does not constitute remaining F-actin from cell entry. Compared with previous reported actin rearrangements around internalized phagosomes, we found that the cocoon shares features with the "actin flashing" phenomenon that occurs target- and cell-unspecific around endocytic compartments to protect cells from overloading degradative pathways (Yam and Theriot, 2004; Liebl and Griffiths, 2009). Both phagosomal actin rearrangements have in common (1) the involvement of certain host proteins such as Arp2/3 (Bierne et al., 2001; Yam and Theriot, 2004), (2) assembly at the cell periphery, and (3) preferably at later formed phagosomes. Besides, *Shigella*'s actin cocoon is clearly distinct and resembles a much longer lasting structure with non-cyclical actin turnover that is much denser than any other cellular actin structure. Its disassembly leads to immediate cytosolic escape of *Shigella*, while actin flashing is followed by vesicle fusion for phagosome maturation (Figure S4E). Therefore, assembly of these distinct actin structures precedes completely different phagosomal fates: actin cocoon assembly correlates with the onset of altered phagosomal maturation and cumulates in a BCV rupture, while actin flashing leads to fusion and bacterial degradation. We propose that *Shigella* hijacks the host actin flashing mechanism for its own needs and thus counteracts a cellular response to invasion.

(E) Deletion of IcsB leads to CDC42 removal from the BCV before rupture but does not prevent its initial recruitment to membrane ruffles.
(F) Quantitative analysis of Cdc42 localization at the BCV of successfully invading *Shigella* with constant (dark blue), transient (light blue), or no (gray) CDC42 localization (n = 311). *Shigella* WT versus Δ*icsB*: constant CDC42, $p < 0.0001$; depleted CDC42, $p < 0.001$; no CDC42, $p < 0.05$.
(G) Recruited TOCA-1 is constantly localized at the BCV dependent on IcsB (infection top: *Shigella* WT; bottom: Δ*icsB*).
Indicated are mean values ± SD of at least 3 independent experiments, in (A) normalized to *Shigella* WT. Statistical significance: Indicated are mean values ± SD. one-way ANOVA (D) or two-way ANOVA with Tukey's multiple-comparisons test (F). Arrow, initial protein recruitment; arrowhead, vacuolar rupture; scale bar: 3 μm. Green bar, protein at BCV; red bar, galectin-3 (Gal-3) at BCV; yellow bar, protein and galectin-3 at BCV remnant; gray bar, no protein or galectin-3. See STAR Methods.

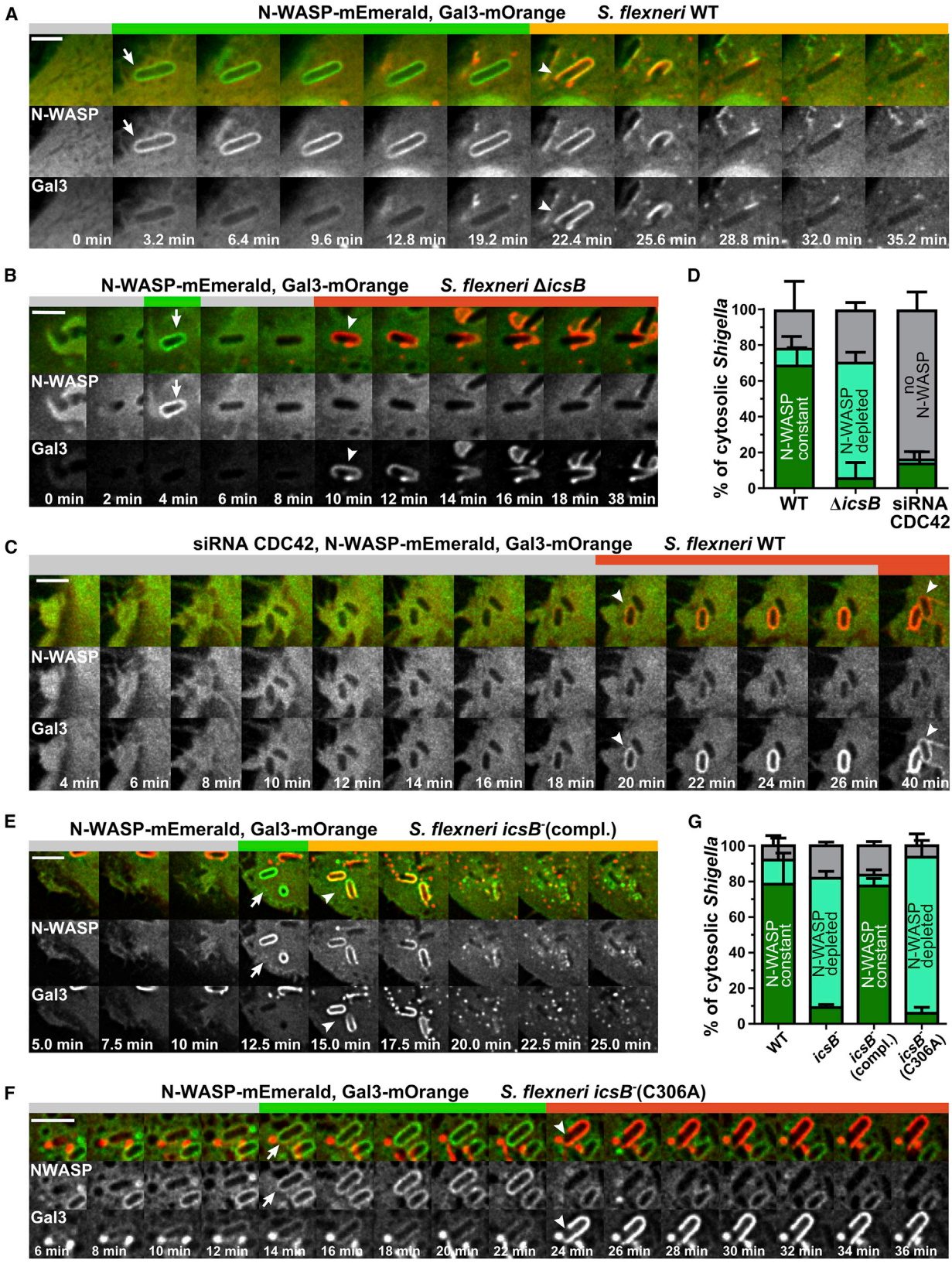

(legend on next page)

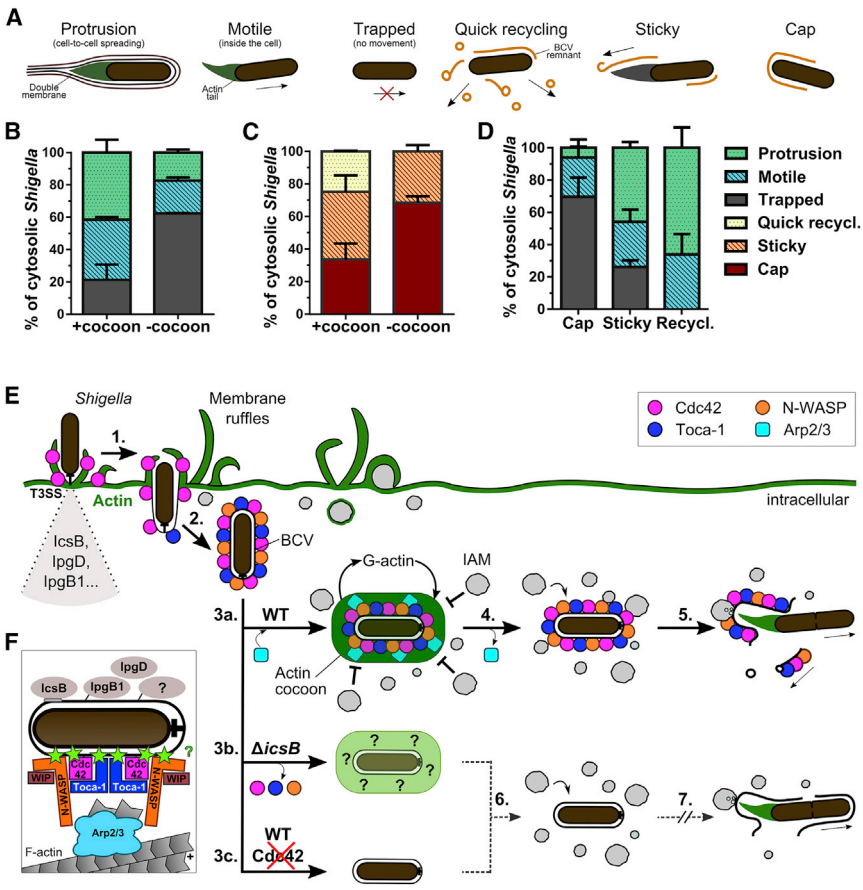

Figure 7. Functional Consequences of Actin Cocoon Formation on Subsequent Infection Steps

(A) Illustration of invading, cytosolic *Shigella* after vacuolar escape and their fates regarding bacterial movement and membrane recycling.

(B–D) Quantification of the motility of individual cytosolic *Shigella* (B) and the fate of their BCV membrane remnants (C). Successive infection steps were monitored 2 h post-infection (p.i.) (see STAR Methods; $n = 144$, mean values ± SD of 6 independent experiments). In most cases, a membrane cap impairs *Shigella* spreading (trapped), while actin cocoon-supported loss of the BCV remnant fosters dissemination (protrusion, motile) (D).

(E) Model for *Shigella*-mediated host actin cytoskeleton subversion by injected T3SS effectors to regulate niche integrity. (1) CDC42 is recruited at the forming BCV. (2) TOCA-1 and N-WASP cluster around the BCV after scission. (3a) Arp2/3 complex recruitment and *de novo* cocoon assembly with constant G-actin turnover. (4) The Arp2/3 complex gets depleted from the BCV during cocoon disassembly, but not CDC42, N-WASP, and TOCA-1. (5) Vacuolar rupture and *Shigella* cytosolic escape after cocoon disassembly. CDC42, N-WASP, and TOCA-1 remain at the recycled BCV remnant. (3b) In the absence of IcsB, these proteins cluster not at the BCV, leading to an altered, actin-containing structure. (3c) Depletion of CDC42 impairs initial N-WASP recruitment and cocoon formation. (6 and 7) Disturbing actin cocoon regulation (3b) or preventing its formation (3c) interferes with vacuolar rupture.

(F) Host factors and *Shigella* effectors involved in cocoon formation. Green star, constant IcsB-dependent localization at the BCV (Figures 5 and 6) and reported (Liu et al., 2018) post-translational lipidation.

Despite this, the endocytic vacuole of *Shigella* is intrinsically different from early endocytic compartments with regard to its molecular composition. We identified a network of host actin regulators that are recruited and prolonged localized at the BCV (Figures 7E and 7F). Interestingly, *Shigella* plays itself an important role in actin cocoon regulation by inducing localized signaling with its effectors IpgD, IpgB1, and IcsB. One strategy to locally induce actin rearrangements is to immobilize key proteins by either (1) increasing their membrane binding affinity or (2) preventing their removal. Both strategies imply subverted host protein localization by *Shigella*. Here, we present a biological function for the recently discovered fatty acyltransferase activity

Figure 6. Constant N-WASP Localization at the BCV Depends on Post-translational Lipidation by IcsB, but CDC42 Is Crucial for Its Initial Recruitment

(A and B) The *Shigella* effector IcsB constantly localizes N-WASP at the BCV during infection after initial IcsB-independent recruitment. Representative time lapses for *Shigella* WT (A) and Δ*icsB* (B) are shown.

(C) CDC42 knockdown strongly impairs initial N-WASP recruitment to the BCV of *Shigella* WT.

(D) Quantification of N-WASP localization at the BCV of invading *Shigella* with constant (dark green), transient (light green), or no (gray) N-WASP ($n = 441$). Statistical significance of *Shigella* WT versus Δ*icsB*: constant N-WASP localization, $p < 0.0001$; N-WASP depleted, $p < 0.0001$; no N-WASP, ns. *Shigella* WT versus siRNA CDC42: constant N-WASP localization, $p < 0.0001$; N-WASP depleted, ns; no N-WASP, $p < 0.0001$.

(E) The complemented *Shigella icsB*$^-$ mutant (*icsB*$^-$[compl.]) clusters N-WASP like *Shigella* WT around the BCV.

(F) In contrast, complementation of *icsB*$^-$ with IcsB lacking fatty acyltransferase activity (*icsB*$^-$ [C306A]) does not restore constant N-WASP localization.

(G) Quantification of N-WASP localization at the BCV of invading *Shigella*, color coded as in (D) ($n = 748$; WT, $n = 138$; *icsB*$^-$, $n = 182$; *icsB*$^-$[compl.], $n = 136$; *icsB*$^-$[C306A], $n = 292$). *Shigella* WT versus *icsB*$^-$: constant N-WASP localization, $p < 0.0001$; N-WASP depleted, $p < 0.0001$; no N-WASP, ns. *Shigella* WT versus *Shigella icsB*$^-$(compl.): constant N-WASP localization, ns; N-WASP depleted, ns; no N-WASP, ns. *Shigella* WT versus *Shigella icsB*$^-$(C306A): constant N-WASP localization, $p < 0.0001$; N-WASP depleted, $p < 0.0001$; no N-WASP, ns.

Statistical significance: two-way ANOVA with Tukey's multiple-comparisons test. Indicated are mean values ± SD of 3 independent experiments. Arrow, initial N-WASP recruitment; arrowhead, moment of vacuolar rupture; scale bars: 3 μm (A–C) and 5 μm (E). Green bar, N-WASP at BCV; red bar, galectin-3 at BCV; yellow bar, N-WASP and galectin-3 at BCV remnant; gray bar, no N-WASP or galectin-3. See STAR Methods and Figure S7.

of IcsB in *Shigella* infection. We found IcsB to be necessary to cluster CDC42, TOCA-1, and N-WASP at *Shigella*'s vacuole, dependent on its lipidation activity. Our findings place IcsB as central *Shigella* effector for the re-localization and entrapment of signaling proteins to regulate cytosolic access. IcsB most likely lipidates its substrates directly at the BCV membrane, as it localizes around intracellular bacteria (Baxt and Goldberg, 2014; Campbell-Valois et al., 2015; Liu et al., 2018). Thus, *Shigella* seems to "glue" host proteins for localized signaling to its endocytic vacuole by adding an additional membrane binding motif. It remains to be further investigated, if all clustered host proteins are directly lipidated by IcsB, or if their constant localization is an indirect effect of either immobilized binding partners or impaired endomembrane trafficking.

Interestingly, IcsB is not required for initial N-WASP localization at the BCV but the Rho GTPase CDC42. This reveals an unexpected second function of active CDC42 during infection besides cellular uptake: it is essential for efficient actin cocoon assembly, which in turn regulates cytosolic access. However, although the vacuolar immobilization of CDC42 depends on IcsB, its initial recruitment, and eventually activation, may involve other effectors targeting upstream Rho signaling during cellular entry. For instance, IpaC may indirectly increase active CDC42 levels via Src signaling (Tran Van Nhieu et al., 1999; Mounier et al., 2009; Adam et al., 1996). IpgB1 is a membrane-bound Rho GEF at intracellular *Shigella* with nucleotide exchange activity for RAC1 and, albeit reduced, CDC42 (Ohya et al., 2005; Huang et al., 2009; Weigele et al., 2017). Consistent with this, we also identified IpgB1, but also IpgD, as an actin cocoon regulator (Figures 5A and 5B). How the inositol-phosphatase IpgD, which produces PI5P from $PI(4,5)P_2$ (Niebuhr et al., 2002; Pendaries et al., 2006), is involved in cocoon assembly remains to be addressed. PI5P leads to PI3K pathway activation (Pendaries et al., 2006) and regulates Rac GEF activity (Viaud et al., 2014). Although our results did not indicate an essential contribution of RAC1 in cocoon assembly, it may have a yet unknown role in infection given its strong localization at the BCV.

Furthermore, we deciphered that actin cocoon dynamics need to be tightly regulated. Cocoon disassembly precedes cytosolic escape, and perturbing its proper regulation by interfering with either cocoon assembly or disassembly consequently diminishes cytosolic invasion of *Shigella*. Remarkably, Δ*ipgB1* and Δ*icsB* mutants had more pronounced cocoons, highlighting the interference of these effectors with actin turnover. Impairing the activation and immobilization of Rho GTPases by deletion of these effectors probably causes a misregulation of the actin cocoon ultrastructure with disturbed actin dynamics. In line with this, we found that the Δ*icsB* BCV differs in its host protein composition from *Shigella* WT. We propose that this induces the formation of a changed cytoskeletal structure less prone to cytosolic escape (Figure 7E). As *Shigella* subverts the host actin cytoskeleton via distinct pathways, deletion of major regulators puts an imbalance in this complex, fine-tuned system.

It emerges that several human pathogens assemble varying actin structures around their intracellular niches. It is tempting to speculate that, as in cells, different structures result in different functions. These actin rearrangements have been associated with maintaining vacuolar stability and integrity, trafficking to acquire nutrients, or preventing phagosome maturation (Kühn and Enninga, 2020). Often, F-actin and additional cytoskeletal systems assemble during late infection steps around the replicative niche of pathogens with long vacuolar lifestyles (Kumar and Valdivia, 2008; Méresse et al., 2001; Sukumaran et al., 2011), like the loose actin meshwork around vacuolar *Salmonella* (Méresse et al., 2001; Vazquez-Torres et al., 2000; Poh et al., 2008; Unsworth et al., 2004).

In contrast, the *Shigella* actin cocoon is clearly distinct, indicating a different function. We found that first cocoon-surrounded BCVs were stationary, excluding a role in actin-driven motility of endocytic compartments (Merrifield et al., 1999; Taunton et al., 2000). Second, a function in sorting and recycling as indicated by dot-like actin structures (Puthenveedu et al., 2010; Seaman et al., 2013) seems unlikely, as actin assembled homogeneously around entire BCVs. Third, we never detected vesicle fusion events with the BCV, nor recruitment of markers for phagosome maturation (Mellouk et al., 2014; Weiner et al., 2016; Kühn et al., 2017) (Figure S4E), eliminating a function in vesicle fusion. We therefore propose two functions of the actin cocoon during *Shigella*'s intracellular lifestyle. We previously demonstrated that the cocoon forms between the BCV and surrounding vesicles (Weiner et al., 2016). Thus, we first suggest that the cocoon acts as "gatekeeper" to regulate pathogen entry into the host cytosol. It shields the BCV as physical barrier from the host endomembrane system and prevents fusion with endosomes and lysosomes, while the cocoon alters its phagosomal identity with regard to lipid and protein composition. Interestingly, CDC42 and Arp2/3 have been reported to prevent phagosome maturation by an F-actin coat around the replicative niche of *Leishmania donovani* (Lodge and Descoteaux, 2005). As cocoon inhibition also delays vacuolar escape, cocoon formation itself may allow proper vacuolar maturation in the presence of macropinosomes. Second, the actin cocoon could prevent host recognition during late infection steps to ensure successful invasion. After vacuolar rupture, it facilitates recycling and removal of the BCV membrane remnants from *Shigella*. The cocoon and its involved molecular machinery could either support vacuolar rupture or eventually govern short distance endomembrane trafficking. It has been shown that LC3, p62, and ubiquitin are recruited to the cytosolic, galectin-3-positive BCV membrane remnants (Dupont et al., 2009) and that cytosolic *Shigella* are trapped by GBPs (Wandel et al., 2017). Additionally, a role of IcsB in autophagy escape by preventing LC3 recruitment to bacteria has been reported (Campbell-Valois et al., 2015; Ogawa et al., 2005; Baxt and Goldberg, 2014). We showed that *Shigella* without cocoon are often surrounded by BCV remnants, causing a high probability of getting trapped inside the cell. We hypothesize that the actin cocoon enables *Shigella* to lose its "danger" signal, which would mark it for autophagy response and degradation.

In conclusion, we discovered a unique microbial subversion strategy: the entrapment of the host actin nucleation machinery by post-translational modification causes localized signaling at the *Shigella* vacuole during early infection. This leads to the formation of an exceptionally thick actin structure to ensure niche integrity and cytosolic escape. The dynamic maturation of this structure must be tightly regulated, as either preventing or disturbing it impairs cytosolic escape.

STAR★METHODS

Detailed methods are provided in the online version of this paper and include the following:

- KEY RESOURCES TABLE
- RESOURCE AVAILABILITY
  - Lead Contact
  - Materials Availability
  - Code Availability
- EXPERIMENTAL MODEL AND SUBJECT DETAILS
  - HeLa and Caco-2 Cells
  - Bacterial strains and culture
- METHOD DETAILS
  - Bacterial infection and immunocytochemistry
  - Plasmids, inhibitors, siRNAs, and transfection
  - Light microscopy
  - FRAP measurement and data analysis
  - Antibodies and western blotting
- QUANTIFICATION AND STATISTICAL ANALYSIS
  - Quantitative image analysis

SUPPLEMENTAL INFORMATION

Supplemental Information can be found online at https://doi.org/10.1016/j.celrep.2020.107638.

ACKNOWLEDGMENTS

For tools and fruitful discussions, we are grateful to John Rohde, Petra Janning, Emmanuel Lemichez, Amel Mettouchi, Claude Parsot, Guy Tran Van Nhieu, Christian Merrifield, Sandrine Etienne-Manneville, Serge Mostowy, Allon Weiner, Yuen-Yan Chang, and Patricia Latour-Lambert. We thank Noelia López-Montero and Laurent Audry for technical support and members of the BCI department for critical discussions. This work was supported by grants from the European Research Council (ERC) (EndoSubvert) to J.E., Agence Nationale de la Recherche (ANR) to J.E. (StopBugEntry) and to C.Z. (ANR-16-CE16-0019-01, NEUROTUNN). J.E. is a member of the LabEx consortium IBEID and MilieuInterieur. S.K. is a recipient of a Pasteur-Roux fellowship.

AUTHOR CONTRIBUTIONS

Conceptualization and Project Administration, S.K. and J.E.; Methodology and Visualization, S.K.; Investigation, S.K. and J.B.; Experimental Help during Revision, M.G. and C.V.; Formal Analysis, S.K. and J.B.; FRAP Analysis, S.L.; Resources, J.E. and C.Z.; Writing – Original Draft, S.K.; Writing – Review & Editing, S.K. and J.E.; Supervision, S.K., L.B., and J.E.; Funding Acquisition, S.K., C.Z., and J.E. All authors discussed the results and commented on the manuscript.

DECLARATION OF INTERESTS

The authors declare no competing interests.

Received: September 30, 2019
Revised: March 10, 2020
Accepted: April 21, 2020
Published: May 12, 2020

REFERENCES

Adam, T., Giry, M., Boquet, P., and Sansonetti, P. (1996). Rho-dependent membrane folding causes Shigella entry into epithelial cells. EMBO J. *15*, 3315–3321.

Baxt, L.A., and Goldberg, M.B. (2014). Host and bacterial proteins that repress recruitment of LC3 to Shigella early during infection. PLoS ONE *9*, e94653.

Bierne, H., Gouin, E., Roux, P., Caroni, P., Yin, H.L., and Cossart, P. (2001). A role for cofilin and LIM kinase in Listeria-induced phagocytosis. J. Cell Biol. *155*, 101–112.

Cai, L., Makhov, A.M., Schafer, D.A., and Bear, J.E. (2008). Coronin 1B antagonizes cortactin and remodels Arp2/3-containing actin branches in lamellipodia. Cell *134*, 828–842.

Campbell-Valois, F.X., Sachse, M., Sansonetti, P.J., and Parsot, C. (2015). Escape of actively secreting Shigella flexneri from ATG8/LC3-positive vacuoles formed during cell-to-cell spread is facilitated by IcsB and VirA. MBio *6*, e02567-14.

Chan, K.T., Creed, S.J., and Bear, J.E. (2011). Unraveling the enigma: progress towards understanding the coronin family of actin regulators. Trends Cell Biol. *21*, 481–488.

Cherfils, J., and Zeghouf, M. (2013). Regulation of small GTPases by GEFs, GAPs, and GDIs. Physiol. Rev. *93*, 269–309.

Cossart, P., and Sansonetti, P.J. (2004). Bacterial invasion: the paradigms of enteroinvasive pathogens. Science *304*, 242–248.

Dupont, N., Lacas-Gervais, S., Bertout, J., Paz, I., Freche, B., Van Nhieu, G.T., van der Goot, F.G., Sansonetti, P.J., and Lafont, F. (2009). Shigella phagocytic vacuolar membrane remnants participate in the cellular response to pathogen invasion and are regulated by autophagy. Cell Host Microbe *6*, 137–149.

Egile, C., Loisel, T.P., Laurent, V., Li, R., Pantaloni, D., Sansonetti, P.J., and Carlier, M.F. (1999). Activation of the CDC42 effector N-WASP by the Shigella flexneri IcsA protein promotes actin nucleation by Arp2/3 complex and bacterial actin-based motility. J. Cell Biol. *146*, 1319–1332.

Ehsani, S., Santos, J.C., Rodrigues, C.D., Henriques, R., Audry, L., Zimmer, C., Sansonetti, P., Tran Van Nhieu, G., and Enninga, J. (2012). Hierarchies of host factor dynamics at the entry site of Shigella flexneri during host cell invasion. Infect. Immun. *80*, 2548–2557.

Etienne-Manneville, S., and Hall, A. (2002). Rho GTPases in cell biology. Nature *420*, 629–635.

Freeman, S.A., and Grinstein, S. (2014). Phagocytosis: receptors, signal integration, and the cytoskeleton. Immunol. Rev. *262*, 193–215.

Gouin, E., Gantelet, H., Egile, C., Lasa, I., Ohayon, H., Villiers, V., Gounon, P., Sansonetti, P.J., and Cossart, P. (1999). A comparative study of the actin-based motilities of the pathogenic bacteria Listeria monocytogenes, Shigella flexneri and Rickettsia conorii. J. Cell Sci. *112*, 1697–1708.

Ho, H.Y., Rohatgi, R., Lebensohn, A.M., Le Ma, Li, J., Gygi, S.P., and Kirschner, M.W. (2004). Toca-1 mediates Cdc42-dependent actin nucleation by activating the N-WASP-WIP complex. Cell *118*, 203–216.

Hoppe, A.D., and Swanson, J.A. (2004). Cdc42, Rac1, and Rac2 display distinct patterns of activation during phagocytosis. Mol. Biol. Cell *15*, 3509–3519.

Huang, Z., Sutton, S.E., Wallenfang, A.J., Orchard, R.C., Wu, X., Feng, Y., Chai, J., and Alto, N.M. (2009). Structural insights into host GTPase isoform selection by a family of bacterial GEF mimics. Nat. Struct. Mol. Biol. *16*, 853–860.

Isberg, R.R., Voorhis, D.L., and Falkow, S. (1987). Identification of invasin: a protein that allows enteric bacteria to penetrate cultured mammalian cells. Cell *50*, 769–778.

Kinoshita, M., Field, C.M., Coughlin, M.L., Straight, A.F., and Mitchison, T.J. (2002). Self- and actin-templated assembly of mammalian septins. Dev. Cell *3*, 791–802.

Kirkbride, K.C., Sung, B.H., Sinha, S., and Weaver, A.M. (2011). Cortactin: a multifunctional regulator of cellular invasiveness. Cell Adhes. Migr. *5*, 187–198.

Kraynov, V.S., Chamberlain, C., Bokoch, G.M., Schwartz, M.A., Slabaugh, S., and Hahn, K.M. (2000). Localized Rac activation dynamics visualized in living cells. Science *290*, 333–337.

Kühn, S., and Enninga, J. (2020). The actin comet guides the way: how Listeria actin subversion has impacted cell biology, infection biology and structural biology. Cell. Microbiol. *22*, e13190.

Kühn, S., and Mannherz, H.G. (2017). Actin: structure, function, dynamics, and interactions with bacterial toxins. Curr. Top. Microbiol. Immunol. *399*, 1–34.

Kühn, S., Lopez-Montero, N., Chang, Y.Y., Sartori-Rupp, A., and Enninga, J. (2017). Imaging macropinosomes during Shigella infections. Methods *127*, 12–22.

Kumar, Y., and Valdivia, R.H. (2008). Actin and intermediate filaments stabilize the Chlamydia trachomatis vacuole by forming dynamic structural scaffolds. Cell Host Microbe *4*, 159–169.

Labigne-Roussel, A.F., Lark, D., Schoolnik, G., and Falkow, S. (1984). Cloning and expression of an afimbrial adhesin (AFA-I) responsible for P blood group-independent, mannose-resistant hemagglutination from a pyelonephritic Escherichia coli strain. Infect. Immun. *46*, 251–259.

Le Clainche, C., and Carlier, M.F. (2008). Regulation of actin assembly associated with protrusion and adhesion in cell migration. Physiol. Rev. *88*, 489–513.

Liebl, D., and Griffiths, G. (2009). Transient assembly of F-actin by phagosomes delays phagosome fusion with lysosomes in cargo-overloaded macrophages. J. Cell Sci. *122*, 2935–2945.

Liu, W., Zhou, Y., Peng, T., Zhou, P., Ding, X., Li, Z., Zhong, H., Xu, Y., Chen, S., Hang, H.C., and Shao, F. (2018). N^{ε}-fatty acylation of multiple membrane-associated proteins by Shigella IcsB effector to modulate host function. Nat. Microbiol. *3*, 996–1009.

Lodge, R., and Descoteaux, A. (2005). Leishmania donovani promastigotes induce periphagosomal F-actin accumulation through retention of the GTPase Cdc42. Cell. Microbiol. *7*, 1647–1658.

Machesky, L.M., Atkinson, S.J., Ampe, C., Vandekerckhove, J., and Pollard, T.D. (1994). Purification of a cortical complex containing two unconventional actins from Acanthamoeba by affinity chromatography on profilin-agarose. J. Cell Biol. *127*, 107–115.

Mavrakis, M., Azou-Gros, Y., Tsai, F.C., Alvarado, J., Bertin, A., Iv, F., Kress, A., Brasselet, S., Koenderink, G.H., and Lecuit, T. (2014). Septins promote F-actin ring formation by crosslinking actin filaments into curved bundles. Nat. Cell Biol. *16*, 322–334.

Mellouk, N., Weiner, A., Aulner, N., Schmitt, C., Elbaum, M., Shorte, S.L., Danckaert, A., and Enninga, J. (2014). Shigella subverts the host recycling compartment to rupture its vacuole. Cell Host Microbe *16*, 517–530.

Méresse, S., Unsworth, K.E., Habermann, A., Griffiths, G., Fang, F., Martínez-Lorenzo, M.J., Waterman, S.R., Gorvel, J.P., and Holden, D.W. (2001). Remodelling of the actin cytoskeleton is essential for replication of intravacuolar Salmonella. Cell. Microbiol. *3*, 567–577.

Merrifield, C.J., Moss, S.E., Ballestrem, C., Imhof, B.A., Giese, G., Wunderlich, I., and Almers, W. (1999). Endocytic vesicles move at the tips of actin tails in cultured mast cells. Nat. Cell Biol. *1*, 72–74.

Mostowy, S., and Cossart, P. (2012). Bacterial autophagy: restriction or promotion of bacterial replication? Trends Cell Biol. *22*, 283–291.

Mostowy, S., Bonazzi, M., Hamon, M.A., Tham, T.N., Mallet, A., Lelek, M., Gouin, E., Demangel, C., Brosch, R., Zimmer, C., et al. (2010). Entrapment of intracytosolic bacteria by septin cage-like structures. Cell Host Microbe *8*, 433–444.

Mostowy, S., Sancho-Shimizu, V., Hamon, M.A., Simeone, R., Brosch, R., Johansen, T., and Cossart, P. (2011). p62 and NDP52 proteins target intracytosolic Shigella and Listeria to different autophagy pathways. J. Biol. Chem. *286*, 26987–26995.

Mounier, J., Laurent, V., Hall, A., Fort, P., Carlier, M.F., Sansonetti, P.J., and Egile, C. (1999). Rho family GTPases control entry of Shigella flexneri into epithelial cells but not intracellular motility. J. Cell Sci. *112*, 2069–2080.

Mounier, J., Popoff, M.R., Enninga, J., Frame, M.C., Sansonetti, P.J., and Van Nhieu, G.T. (2009). The IpaC carboxyterminal effector domain mediates Src-dependent actin polymerization during Shigella invasion of epithelial cells. PLoS Pathog. *5*, e1000271.

Mullins, R.D., Heuser, J.A., and Pollard, T.D. (1998). The interaction of Arp2/3 complex with actin: nucleation, high affinity pointed end capping, and formation of branching networks of filaments. Proc. Natl. Acad. Sci. USA *95*, 6181–6186.

Niebuhr, K., Giuriato, S., Pedron, T., Philpott, D.J., Gaits, F., Sable, J., Sheetz, M.P., Parsot, C., Sansonetti, P.J., and Payrastre, B. (2002). Conversion of PtdIns(4,5)P(2) into PtdIns(5)P by the S.flexneri effector IpgD reorganizes host cell morphology. EMBO J. *21*, 5069–5078.

Niedergang, F., and Grinstein, S. (2018). How to build a phagosome: new concepts for an old process. Curr. Opin. Cell Biol. *50*, 57–63.

Ogawa, M., Yoshimori, T., Suzuki, T., Sagara, H., Mizushima, N., and Sasakawa, C. (2005). Escape of intracellular Shigella from autophagy. Science *307*, 727–731.

Ohya, K., Handa, Y., Ogawa, M., Suzuki, M., and Sasakawa, C. (2005). IpgB1 is a novel Shigella effector protein involved in bacterial invasion of host cells. Its activity to promote membrane ruffling via Rac1 and Cdc42 activation. J. Biol. Chem. *280*, 24022–24034.

Onodera, N.T., Ryu, J., Durbic, T., Nislow, C., Archibald, J.M., and Rohde, J.R. (2012). Genome sequence of Shigella flexneri serotype 5a strain M90T Sm. J. Bacteriol. *194*, 3022.

Paz, I., Sachse, M., Dupont, N., Mounier, J., Cederfur, C., Enninga, J., Leffler, H., Poirier, F., Prevost, M.C., Lafont, F., and Sansonetti, P. (2010). Galectin-3, a marker for vacuole lysis by invasive pathogens. Cell. Microbiol. *12*, 530–544.

Pendaries, C., Tronchère, H., Arbibe, L., Mounier, J., Gozani, O., Cantley, L., Fry, M.J., Gaits-Iacovoni, F., Sansonetti, P.J., and Payrastre, B. (2006). PtdIns5P activates the host cell PI3-kinase/Akt pathway during Shigella flexneri infection. EMBO J. *25*, 1024–1034.

Poh, J., Odendall, C., Spanos, A., Boyle, C., Liu, M., Freemont, P., and Holden, D.W. (2008). SteC is a Salmonella kinase required for SPI-2-dependent F-actin remodelling. Cell. Microbiol. *10*, 20–30.

Pollard, T.D. (2016). Actin and actin-binding proteins. Cold Spring Harb. Perspect. Biol. *8*, a018226.

Puthenveedu, M.A., Lauffer, B., Temkin, P., Vistein, R., Carlton, P., Thorn, K., Taunton, J., Weiner, O.D., Parton, R.G., and von Zastrow, M. (2010). Sequence-dependent sorting of recycling proteins by actin-stabilized endosomal microdomains. Cell *143*, 761–773.

Ray, K., Bobard, A., Danckaert, A., Paz-Haftel, I., Clair, C., Ehsani, S., Tang, C., Sansonetti, P., Tran, G.V., and Enninga, J. (2010). Tracking the dynamic interplay between bacterial and host factors during pathogen-induced vacuole rupture in real time. Cell. Microbiol. *12*, 545–556.

Revenu, C., Courtois, M., Michelot, A., Sykes, C., Louvard, D., and Robine, S. (2007). Villin severing activity enhances actin-based motility in vivo. Mol. Biol. Cell *18*, 827–838.

Rohatgi, R., Ma, L., Miki, H., Lopez, M., Kirchhausen, T., Takenawa, T., and Kirschner, M.W. (1999). The interaction between N-WASP and the Arp2/3 complex links Cdc42-dependent signals to actin assembly. Cell *97*, 221–231.

Romero, S., Quatela, A., Bornschlögl, T., Guadagnini, S., Bassereau, P., and Tran Van Nhieu, G. (2012). Filopodium retraction is controlled by adhesion to its tip. J. Cell Sci. *125*, 4999–5004.

Rottner, K., Faix, J., Bogdan, S., Linder, S., and Kerkhoff, E. (2017). Actin assembly mechanisms at a glance. J. Cell Sci. *130*, 3427–3435.

Santos, J.C., and Enninga, J. (2016). At the crossroads: communication of bacteria-containing vacuoles with host organelles. Cell. Microbiol. *18*, 330–339.

Schnupf, P., and Sansonetti, P.J. (2019). *Shigella* pathogenesis: new insights through advanced methodologies. Microbiol. Spectr. *7* (*2*).

Schroeder, G.N., and Hilbi, H. (2008). Molecular pathogenesis of Shigella spp.: controlling host cell signaling, invasion, and death by type III secretion. Clin. Microbiol. Rev. *21*, 134–156.

Seaman, M.N., Gautreau, A., and Billadeau, D.D. (2013). Retromer-mediated endosomal protein sorting: all WASHed up!. Trends Cell Biol. *23*, 522–528.

Sidik, S., Kottwitz, H., Benjamin, J., Ryu, J., Jarrar, A., Garduno, R., and Rohde, J.R. (2014). A Shigella flexneri virulence plasmid encoded factor controls production of outer membrane vesicles. G3 (Bethesda) *4*, 2493–2503.

Sirianni, A., Krokowski, S., Lobato-Márquez, D., Buranyi, S., Pfanzelter, J., Galea, D., Willis, A., Culley, S., Henriques, R., Larrouy-Maumus, G., et al.

(2016). Mitochondria mediate septin cage assembly to promote autophagy of Shigella. EMBO Rep. *17*, 1029–1043.

Sukumaran, B., Mastronunzio, J.E., Narasimhan, S., Fankhauser, S., Uchil, P.D., Levy, R., Graham, M., Colpitts, T.M., Lesser, C.F., and Fikrig, E. (2011). Anaplasma phagocytophilum AptA modulates Erk1/2 signalling. Cell. Microbiol. *13*, 47–61.

Suzuki, T., Miki, H., Takenawa, T., and Sasakawa, C. (1998). Neural Wiskott-Aldrich syndrome protein is implicated in the actin-based motility of Shigella flexneri. EMBO J. *17*, 2767–2776.

Taunton, J., Rowning, B.A., Coughlin, M.L., Wu, M., Moon, R.T., Mitchison, T.J., and Larabell, C.A. (2000). Actin-dependent propulsion of endosomes and lysosomes by recruitment of N-WASP. J. Cell Biol. *148*, 519–530.

Taylor, M.J., Perrais, D., and Merrifield, C.J. (2011). A high precision survey of the molecular dynamics of mammalian clathrin-mediated endocytosis. PLoS Biol. *9*, e1000604.

Tran Van Nhieu, G., Caron, E., Hall, A., and Sansonetti, P.J. (1999). IpaC induces actin polymerization and filopodia formation during Shigella entry into epithelial cells. EMBO J. *18*, 3249–3262.

Unsworth, K.E., Way, M., McNiven, M., Machesky, L., and Holden, D.W. (2004). Analysis of the mechanisms of Salmonella-induced actin assembly during invasion of host cells and intracellular replication. Cell. Microbiol. *6*, 1041–1055.

Valencia-Gallardo, C.M., Carayol, N., and Tran Van Nhieu, G. (2015). Cytoskeletal mechanics during Shigella invasion and dissemination in epithelial cells. Cell. Microbiol. *17*, 174–182.

Vazquez-Torres, A., Xu, Y., Jones-Carson, J., Holden, D.W., Lucia, S.M., Dinauer, M.C., Mastroeni, P., and Fang, F.C. (2000). Salmonella pathogenicity island 2-dependent evasion of the phagocyte NADPH oxidase. Science *287*, 1655–1658.

Vetter, I.R., and Wittinghofer, A. (2001). The guanine nucleotide-binding switch in three dimensions. Science *294*, 1299–1304.

Viaud, J., Lagarrigue, F., Ramel, D., Allart, S., Chicanne, G., Ceccato, L., Courilleau, D., Xuereb, J.M., Pertz, O., Payrastre, B., and Gaits-Iacovoni, F. (2014). Phosphatidylinositol 5-phosphate regulates invasion through binding and activation of Tiam1. Nat. Commun. *5*, 4080.

Wandel, M.P., Pathe, C., Werner, E.I., Ellison, C.J., Boyle, K.B., Von Der Malsburg, A., Rohde, J., and Randow, F. (2017). GBPs inhibit motility of Shigella flexneri but are targeted for degradation by the bacterial ubiquitin ligase IpaH9.8. Cell Host Microbe *22*, 507–518.e5.

Weigele, B.A., Orchard, R.C., Jimenez, A., Cox, G.W., and Alto, N.M. (2017). A systematic exploration of the interactions between bacterial effector proteins and host cell membranes. Nat. Commun. *8*, 532.

Weiner, A., Mellouk, N., Lopez-Montero, N., Chang, Y.Y., Souque, C., Schmitt, C., and Enninga, J. (2016). Macropinosomes are key players in early Shigella invasion and vacuolar escape in epithelial cells. PLoS Pathog. *12*, e1005602.

Yam, P.T., and Theriot, J.A. (2004). Repeated cycles of rapid actin assembly and disassembly on epithelial cell phagosomes. Mol. Biol. Cell *15*, 5647–5658.

STAR★METHODS

KEY RESOURCES TABLE

REAGENT OR RESOURCE	SOURCE	IDENTIFIER
Antibodies		
polyclonal rabbit anti-Septin 7	IBL	Cat#18991; RRID: AB_10705434
monoclonal mouse anti-β-actin	Sigma-Aldrich	Cat#A5316; RRID: AB_476743
monoclonal mouse anti-CDC42	BD Transduction Laboratories	Cat#610929; RRID: AB_398244
monoclonal mouse anti-ArpC3 p21-Arc Clone26	BD Transduction Laboratories	Cat#612234; RRID: AB_399557
monoclonal mouse anti-RAC1 clone 23A8	Abcam	Cat# ab33186; RRID: AB_777598
anti-mouse horseradish peroxidase-conjugated	Bio-Rad	Cat#170-6516; RRID: AB_11125547
anti-rabbit horseradish peroxidase-conjugated	Bio-Rad	Cat#170-6515; RRID: AB_11125142
Bacterial strains		
Shigella flexneri (WT) 5a M90T-Sm virulence plasmid pWR100 (GenBank#CM001474.1, GenBank#AL391753.1)	Philippe Sansonetti John R. Rohde	(Onodera et al., 2012)
S. flexneri icsB^{-} (non-polar *icsB* mutant)	Claude Parsot	N/A
S. flexneri icsB^{-}(compl.) (*icsB*$^{-}$ mutant carrying pUC8::*icsB-ipgA* expressing IcsB and its chaperone IpgA)	Claude Parsot	N/A
S. flexneri icsB^{-}(C306A) (*icsB*$^{-}$ mutant carrying pUC8::*icsB(C306A)-ipgA* expressing enzymatic inactive IcsB-C306A and its chaperone IpgA)	This work	N/A
S. flexneri (WT) mCherry (expressing mCherry and Afa-I (*E. coli* pIL22))	Guy Tran Van Nhieu	N/A
S. flexneri (WT) (expressing Afa-I (afaE gene) from *E. coli*)	John R. Rohde	(Labigne-Roussel et al., 1984)
S. flexneri (WT) DsRed (expressing dsRed and Afa-I)	Yuen-Yan Chang	N/A
S. flexneri Δ*icsA* (Δ*icsA::tetRA* expressing Afa-I)	John R. Rohde	(Sidik et al., 2014)
S. flexneri Δ*ipgB1* (Δ*ipgB1::tetRA* expressing Afa-I)	John R. Rohde	(Sidik et al., 2014)
S. flexneri Δ*ipgD* (Δ*ipgD::tetRA* expressing Afa-I)	John R. Rohde	(Sidik et al., 2014)
S. flexneri Δ*ipaJ* (Δ*ipaJ::tetRA* expressing Afa-I)	John R. Rohde	(Sidik et al., 2014)
S. flexneri Δ*ospG* (Δ*ospG::tetRA* expressing Afa-I)	John R. Rohde	(Sidik et al., 2014)
S. flexneri Δ*ospC1* (Δ*ospC1::tetRA* expressing Afa-I)	John R. Rohde	(Sidik et al., 2014)
S. flexneri Δ*virA* (Δ*virA::tetRA* expressing Afa-I)	John R. Rohde	(Sidik et al., 2014)
S. flexneri Δ*ipaH7.8* (Δ*ipaH7.8::tetRA* expressing Afa-I)	John R. Rohde	(Sidik et al., 2014)
Escherichia coli DH5α	Thermo Fisher Scientific	Cat#18265017
Escherichia *coli* InvA (expressing *Yersinia* invasin A)	Guy Tran Van Nhieu	N/A
Salmonella enterica serovar Typhimurium (*S.* Typhimurium) SL1344 / pGG2-dsRed (WT)	ATCC	ATCC SL1344
Chemicals, Peptides, and Recombinant Proteins		
X-tremeGENE 9 DNA transfection reagent	Roche	Cat#6365779001
Lipofectamine RNAiMAX	Invitrogen	Cat#13778030
DAPI	Thermo Fisher Scientific	Cat#D1306
Alexa Fluor 647 Phalloidin	Thermo Fisher	Cat#A22287
Paraformaldehyde 16%	Electron Microscopy Sciences	Cat#15710
Ampicillin	Sigma-Aldrich	Cat#A9393
Kanamycin	Sigma-Aldrich	Cat#K1377
Isopropyl-β-D-thiogalactoside (IPTG)	Sigma-Aldrich	Cat#10724815001
Poly-L-lysine	Sigma-Aldrich	Cat#P4707
Agarose	Invitrogen	Cat#16500-500

(*Continued on next page*)

Continued

REAGENT OR RESOURCE	SOURCE	IDENTIFIER
Dulbecco's Modified Eagle's Medium, High Glucose, GlutaMax	Thermo Fisher Scientific	Cat#10566016
Fetal Bovine Serum	Sigma-Aldrich	Cat#F7524
DPBS	Thermo Fisher Scientific	Cat#14190144
MEM Non-Essential Amino Acids Solution	Thermo Fisher Scientific	Cat#11140050
HEPES	Thermo Fisher Scientific	Cat#15630080
0.05% Trypsin-EDTA	Thermo Fisher Scientific	Cat#25300054
ProLong Gold Antifade Mountant	ThermoFisher Scientific	Cat#P10144
FluoroBrite DMEM	ThermoFisher Scientific	Cat#A1896701
Complete Protease Inhibitor	Roche	Cat#11836170001
RIPA buffer	ThermoFisher Scientific	Cat#89901
NuPAGE 4-12% Bis-Tris Protein Gels	Thermo Fisher Scientific	Cat#NP0321BOX
Micro BCA™ Protein Assay Kit	Thermo Fisher Scientific	Cat#23235
Trans-Blot® Turbo RTA Mini Nitrocellulose Transfer Kit	Bio-Rad	Cat#1704270
Trans-Blot© Turbo Transfer System	Bio-Rad	Cat#1704150
SuperSignal West Pico PLUS Chemiluminescent Substrate	Thermo Scientific	Cat#34577
QIAprep Spin Miniprep Kit	QIAGEN	Cat# 27106
Q5® Site Directed mutagenesis kit	New Englands Biolabs	Cat#E0554S
Inhibitors		
Cytochalasin D	Enzo Life Sciences Inc	Cat#BML-T109-0001
SMIFH2	Sigma	Cat#S4826
Y-27632	BD biosciences	Cat#562822
NSC23766	Calbiochem	Cat#553502
(±)-Blebbistatin	BioVision	Cat#BV-2405-5
Wortmannin	Enzo Life Sciences Inc	Cat#BML-ST415-0001
CK666	Sigma	Cat#SML0006
ETH1864	Tocris Bioscience	Cat#3872
ML141	Tocris Bioscience	Cat#71203-35-5
Experimental Models: Cell Lines		
HeLa Human cervix carcinoma epithelial cell line clone CCL-2	ATCC	Cat#11033106
Caco-2 TC7 cells	Philippe Sansonetti	N/A
HeLa cells stably expressing galectin-3-mOrange	Patricia Latour-Lambert	N/A
Oligonucleotides		
ON-TARGETplus Non-targeting Control Pool	Dharmacon	Cat#D-001810-10-05
SEPT7 siRNA	Ambion	Cat#s2743
ON-TARGETplus SMARTpool CDC42	Dharmacon	Cat#L-005057-00-0005
ON-TARGETplus SMARTpool ARPC3	Dharmacon	Cat#L-005284-00-0005
ON-TARGETplus SMARTpool RAC1	Dharmacon	Cat#L-003560-00-0005
Recombinant DNA		
pmCherryC1-Arp3	Christian Merrifield	(Taylor et al., 2011) Addgene Cat#27682
pmCherryC1- Cortactin	Christian Merrifield	(Taylor et al., 2011) Addgene Cat#27676
pmCherryC1-Cofilin	Christian Merrifield	(Taylor et al., 2011) Addgene Cat#27687
pEYFP-C1-Villin	Sylvie Robine	(Revenu et al., 2007)
pEGFP-C1-TOCA-1	Jennifer Gallop	N/A

(*Continued on next page*)

Continued

REAGENT OR RESOURCE	SOURCE	IDENTIFIER
pGFP-Cortactin	Kenneth Yamada	Addgene Cat#50728
mEmerald-N-WASP-C-18	Michael Davidson	Addgene Cat#54199
mEmerald-Coronin1B	Michael Davidson	Addgene Cat#54050
pmCherry-C1-WIP	Anna Huttenlocher	Addgene Cat#29573
pEGFP-Actin	(Mounier et al., 2009)	N/A
mCherry-Actin	Dominique Lallemand	N/A
pOrange-C3-Actin	(Ehsani et al., 2012)	N/A
pEGFP-Galectin-3	(Paz et al., 2010)	N/A
pOrange-Galectin-3	(Ray et al., 2010)	N/A
mTurquoise-Galectin-3	Noelia Lopez-Montero	N/A
pmCherry-CDC42	Sandrine Etienne-Manneville	N/A
pEYFP-CDC42	Joel Swanson	(Hoppe and Swanson, 2004)
GFP-CDC42-V12	Sandrine Etienne-Manneville	N/A
GFP-CDC42-N17	Sandrine Etienne-Manneville	N/A
pcDNA3-EGFP-RAC1	Klaus Hahn (Kraynov et al., 2000)	Addgene Cat#13719
pEYFP-RHOA	Joel Swanson	(Hoppe and Swanson, 2004)
pGFP-2XFYVE	Philippe Benaroch	N/A
pmCherry-2xFYVE	Harald Stenmark and Kay Oliver Schink	N/A
pEYFP-LAMP1	Walther Mothes	Addgene Cat#1816
pEGFP-LC3B	Thomas Wollert	N/A
pmCherry-RAB7	Michael Davidson	Addgene Cat#55127
Software and Algorithms		
FIJI	NIH	https://fiji.sc https://imagej.net/ImageJ
Volocity 6.3 PerkinElmer	PerkinElmer	N/A
NIS-Elements Microscope Imaging Software	Nikon	N/A
GraphPad Prism	GraphPad Software v6.0, La Jolla, USA	https://www.graphpad.com/
Excel	Microsoft	N/A
ICY	Institut Pasteur	http://icy.bioimageanalysis.org/
Inkscape	Version 0.92.3	https://inkscape.org/
Other		
Zeiss LSM780 Elyra PS1 microscope equipped with the followings:	Zeiss	N/A
63x/1.4 oil Plan Apo objective	Zeiss	N/A
EMCCD Andor Ixon 887 1K camera	Andor	N/A
Perkin Elmer UltraView spinning disk confocal microscope equipped with the followings:	Perkin Elmer	N/A
60 × /1.3 oil objective	Nikon	N/A
PSU C910-50 camera	Hamamatsu	N/A
Inverted widefield microscope equipped with the followings:	Nikon	N/A
20x/0.5NA air objective	Nikon	N/A
CoolSnap2 camera	Roeper Scientific	N/A
DeltaVision Elite epifluorescence microscope	GE Healthcare	N/A
96-well cell culture microplates with clear flat bottom	Greiner Bio One International	Cat#655090
Precision cover glasses thickness No. 1.5H	Marienfeld Superior	Cat#0117580
35 mm glass bottom μ-Dishes	Ibidi	Cat#81158
Tissue culture flask 75	TPP	Cat#90076
Costar® 6-well Clear TC-treated Multiple Well Plates	Corning	Cat#3516

RESOURCE AVAILABILITY

Lead Contact

Further information and requests for resources and reagents should be directed to and will be fulfilled by the lead contact, Jost Enninga (jost.enninga@pasteur.fr).

Materials Availability

We are glad to share all reagents generated in this study without restriction. Please contact the lead contact (jost.enninga@pasteur.fr) without restriction.

Code Availability

The published article includes all datasets analyzed during this study. Please contact the lead author in case you require the original source data, for example time-lapse series that cannot be added to a public database.

EXPERIMENTAL MODEL AND SUBJECT DETAILS

HeLa and Caco-2 Cells

Human epithelial HeLa cells (clone CCL-2, ATCC #11033106), HeLa cells stably expressing galectin-3-mOrange (Patricia Latour-Lambert), and intestinal epithelial Caco-2 TC7 cells (kindly provided by P. Sansonetti) were cultured in Dulbecco's modified Eagle's medium (DMEM, Thermo Fisher Scientific #10566016) supplemented with 10% (v/v) heat-inactivated fetal bovine serum (FBS, Sigma-Aldrich #F7524) at 37°C, 5% (HeLa) or 10% (Caco-2) CO_2. Cell lines were checked negative for mycoplasma.

Bacterial strains and culture

The following streptomycin-resistant *Shigella flexneri* 5a M90T-Sm (GenBank #CM001474.1) derived strains harboring the pWR100 virulence plasmid (GenBank #AL391753.1) were used: wild-type M90T (WT), M90T (WT) containing the afimbrile adhesin E gene (afaE) from *E. coli* (Labigne-Roussel et al., 1984), M90T (WT) expressing dsRed and AfaI (Yuen-Yan Chang). The screened library of *S. flexneri* single deletion T3SS effector mutants was kindly provided by John R. Rohde (Dalhousie University) as part of a pWR100 collection originating from M90T (WT) AfaI (Sidik et al., 2014). We used *Salmonella enterica* serovar Typhimurium (*S.* Typhimurium) strain SL1344 pGG2-dsRed (WT) expressing dsRed. The *E. coli* InvA strain containing the *Yersinia* invasin A (Isberg et al., 1987) and *S. flexneri* M90T (WT) expressing mCherry and AfaI (*E. coli* plasmid pIL22) were provided by Guy Tran Van Nhieu. *S. flexneri icsB*$^-$ and *S. flexneri icsB*$^-$(compl.) (pUC8::*icsB-ipgA*, expressing IcsB and its chaperone IpgA) were provided by Claude Parsot. *S. flexneri* strains were grown in trypticase soy broth (TCSB) with 50 μg/ml ampicillin, and cultured at 37°C on TCSB agar including 0.01% congo red to select for functional T3SS system. *S.* Typhimurium was grown at 37°C in lysogeny broth (LB) medium supplemented with 0.3 M NaCl and 50 μg/ml ampicillin, while *E. coli* InvA was cultured in LB medium with 100 μg/ml ampicillin. *E. coli* DH5α and derivatives were grown at 37°C in LB medium, when needed the medium was supplemented with 100 μg/ml ampicillin.

METHOD DETAILS

Bacterial infection and immunocytochemistry

HeLa cells were used for all experiments except Figures S1B and S7B. All infection assays were performed in EM buffer (120 mM NaCl, 7 mM KCl, 1.8 mM $CaCl_2$, 0.8 mM $MgCl_2$, 5 mM glucose, 25 mM HEPES, pH 7.3). Actin cocoon formation and vacuolar escape was not affected by EM buffer compared to FluoroBrite DMEM (Thermo Fisher Scientific #A1896701) supplemented with 10% heat-inactivated FBS and 4 mM GlutaMAX (Thermo Fisher Scientific #35050061). For *Shigella*, infection cultures in TCBS plus antibiotics (and ITPG 2 mM for complementation assays) were inoculated with a 1:100 dilution of an overnight culture and incubated at 37°C to an optical density (OD 600 nm) of 0.6-0.7. Then, bacteria were washed in PBS and resuspended in EM buffer. Strains without Afa-I adhesin were incubated for 20 min with poly-L-lysine (Sigma, #P4707) as described previously (Weiner et al., 2016). All *Shigella*-containing experiments were performed with Afa-I strains, besides experiments shown in Figures 6E–6G and S7F–S7H, which were performed with poly-L-lysine-coated *Shigella*. For complementation, the infection cultures of *Shigella icsB*$^-$(compl.) and *icsB*$^-$(C306A) strains were grown in 2 mM ITPG before invasion assays. In general, bacterial dilutions were prepared for the following MOIs: live imaging 96-well format MOI 5-150 (normally MOI in range 15-40 to exclude effects of phagocytic load), live imaging 35 mm glass bottom μ-Dishes (Ibidi, #81158) MOI 15 and poly-L-lysine treated bacteria MOI 50. Other bacterial pathogens, like *Salmonella* or *E. coli* InvA, were grown similarly in their corresponding medium. *Salmonella* infections at MOI 50 were started maximal 10 min after spinning down the bacteria in pre-heated Eppendorf tubes and washing in pre-heated EM buffer. *E. coli* InvA were added to imaged cells at an MOI of 50. For fixed experiments, *Shigella* (WT) DsRed adhered for 10 minutes at 20°C (MOI 50), before incubation at 37°C for 45 min or 60 min. Samples were washed three times with PBS, fixed in cold 2% PFA, and stained with Alexa Fluor 647 Phalloidin (Thermo Fisher Scientific, #A22287) for 45 min.

Plasmids, inhibitors, siRNAs, and transfection

The following plasmids were kindly provided by our colleagues: Arp3-pmCherryC1, Cortactin-pmCherryC1, as well as Cofilin-pmCherryC1 from Christian Merrifield (Taylor et al., 2011), CDC42-mCherry, CDC42-V12-GFP, as well as CDC42-N17-GFP from Sandrine Etienne-Manneville, pEYFP-C1-Villin from Sylvie Robine (Revenu et al., 2007), pEGFP-C1-TOCA-1 from Jennifer Gallop, pGFP-Cortactin from Kenneth Yamada, mEmerald-N-Wasp-C-18, mEmerald-Coronin1B and pmCherry-RAB7 from Michael Davidson, pmCherry-C1-WIP from Anna Huttenlocher, pEYFP-CDC42 and pEYFP-RHOA from Joel Swanson (Hoppe and Swanson, 2004), pcDNA3-EGFP-RAC1 from Klaus Hahn (Kraynov et al., 2000), pGFP-2XFYVE from Philippe Benarock, pmCherry-2xFYVE from Harald Stenmark, pEYFP-LAMP1 from Walther Mothes, and pEGFP-LC3 from Thomas Wollert. The plasmids pEGFP-C3-Actin, pOrange-C3-Actin, pEGFP-N1-Galectin-3, and pOrange-Galectin-3 have been described previously (Paz et al., 2010; Mounier et al., 2009) (Ehsani et al., 2012) (Ray et al., 2010). All plasmid constructs were verified by sequencing. For quantitative screening experiments (Figures 1F, 1G, 3B–3D, 4E, 4F, 5A, 5B, S1E–S1G, S2, S5F–S5J, S6C, and S6D), HeLa cells were seeded at a density of 7000 cells/well 24 h prior to transfection into 96-well plates (Greiner, #655090). Cells were then transfected with the respective plasmids using X-tremeGENE 9 DNA transfection reagent (Roche, #6365779001) for 48 h (24 h for TOCA-1 and CDC42).

pUC8::*icsB*(C306A)-*ipgA* construction: Mutagenesis to inactivate IcsB enzymatic activity in the pUC derivative was performed using the Q5® Site Directed mutagenesis kit (New Englands Biolabs #E0554S) as suggested by the manufacturer. Mutagenesis primers were icsB_C306_F (ATCTGAAAACgcTGCTGGTATGGCAC) and icsB_C306_R (TTACTGATTAATTTATAATTTGCC). First, plasmid was divergently amplified using mutagenesis primers and Pfu polymerase from the kit. Next, the template plasmid was digested with DpnI and the PCR product phosphorylated and ligated using the KLD enzyme mix according to the manufacturer instructions. Ligation products were transformed in chemocompentent *E. coli* DH5α and transformants were selected in LB agar supplemented with 100 μg/mL of ampicillin. Plasmids were purified using the QIAprep Spin Miniprep Kit according to the manufacturer instructions and verified by sequencing.

In inhibitor screens, the following compounds and concentrations (DMSO stock solutions dissolved in EM buffer) were applied: 1 μM Cytochalasin D (Enzo Life Sciences Inc, #BML-T109-0001), 10 μM SMIFH2 (Sigma-Aldrich, #S4826), 5 μM ML141 (Tocris Bioscience, #71203-35-5; of note: we observed solubility limitations with this inhibitor, therefore the effective concentration will be lower), 25 μM ETH1864 (Tocris Bioscience, #3872), 15 μM Y-27632 (BD biosciences, #562822), 50 μM NSC23766 (Calbiochem, #553502), 15 μM (±)-Blebbistatin (BioVision, #BV-2405-5), 10 μM Wortmannin (Enzo Life Sciences Inc, #BML-ST415-0001), 200 μM CK666 (Sigma, #SML0006). For each inhibitor, working concentrations were identified that did not affect cell viability in the duration of the experiment, but showed clear effects on either cell shape or actin rearrangements during infection. In general, cells were pre-incubated for 40 min at 37°C in EM buffer containing the corresponding inhibitor. Afterward, bacteria were added in EM buffer with the same inhibitor concentration and imaged immediately. For Cytochalasin D, cells were not pre-incubated and the inhibitor was added with the bacteria.

Following siRNAs were used in siRNA transfections: 50 nM SEPT7 (ID #s2743, Ambion), 10 nM ON-TARGETplus SMARTpool siRNAs from Dharmacon for CDC42 (#L-005057-00-0005), ARPC3 (#L-005284-00-0005), RAC1 (#L-003560-00-0005) as well as Non-targeting pool as negative control (#D-001810-10-05). For quantitative analysis (Figures 2B, 4D, 4F, S5A–S5E, and S6B), HeLa cells were seeded at a density of 5000 cells/well 24 h prior to transfection into 96-well plates. Reverse siRNA transfection was performed using the Lipofectamine RNAiMAX Transfection Reagent (Invitrogen, #13778030) for 72 h. After 48 h, transfection mixes were removed and cells were transfected for 24 h with pEGFP-C3-actin and pOrange-Galectin3 plasmids using X-tremeGENE 9 DNA transfection reagent. In parallel, upscaled samples for western blot quantification were prepared in 6-well plates and for live imaging at the DeltaVision wide-field microscope in 35 mm glass bottom μ-Dishes (Ibidi, #81158) (Figures 4A–4C, 6C, 6D, S3A, and S6A).

Light microscopy

For quantitative screening experiments (Figures 1F, 1G, 2B, 3B–3D, 4D–4F, 5A, 5B, S1E–S1G, S2, S5, and S6B–S6D), image acquisition was performed using an inverted epifluorescence Nikon Ti-E widefield microscope with a 20x (0.5 Numerical Aperture (NA), 2.1 Working Distance (WD)) N-Plan air objective, an automatic programmable xy stage, and the Nikon perfect focus system. Cells were imaged every 1-2 min for 2-3 h inside a 37°C heating chamber. *Shigella* (WT) infections were monitored as control in each experiment. To detect host protein recruitment to *Shigella*-induced endocytic compartments (BCV, IAMs), time-lapse movies of high resolution were recorded at 37°C on a DeltaVision Elite (GE Healthcare) widefield microscope using a 60 × /1.42 NA oil objective and a step size of 0.25-0.35 μm (Figures 1A–1C, 2A, 2C–2H, 3E, 4A–4C, 5C–5G, 6, 7B, S1C, S2A, S4, S6A, S6E, and S7; Videos S1 and S2). Imaging was performed for 2-3 h after adding the bacteria and the frequency of image acquisition was adjusted to the dynamics of the investigated event. Images were subsequently deconvolved using an integrated deconvolution analysis software (DeltaVision Elite). Bleach correction of illustrated images was performed using Fiji (http://fiji.sc). Fixed samples were imaged using a Perkin Elmer UltraView spinning disc confocal microscope, with a 60X × /1.3 N.A. oil objective and a Z step size of 0.3 μm (Figures S1A and S1B).

FRAP measurement and data analysis

Live-cell FRAP experiments (Figures 1D and 1E; Videos S3, S4, and S5) were performed at an inverted Perkin Elmer UltraView VOX confocal spinning disk microscope equipped with a FRAP module and Volocity software. Images were acquired using a 60X × /1.3 N.A. oil objective with a single Z plane. Cells expressing actin-GFP in 35 mm glass bottom culture dishes were imaged at 37°C in EM

buffer. Cells were infected with *Shigella* (WT) DsRed and bacterial presence was controlled before bleaching of each single cocoon structure. We monitored the fluorescence of GFP-actin using low intensity laser excitation (488 nm) (pre-bleach scans). A circular region was photobleached with the same laser excitation at high intensity (decrease of the fluorescence into the ROI by 60%–80%), and fluorescence recovery monitored over time (post-bleach scans). 10 pre-bleach images were recorded at 1 s intervals, followed by a single bleaching pulse. One cocoon per cell was bleached with only half-bleached ones considered for analysis. The duration of post-bleach imaging was adjusted to the duration of fluorescence recovery. Actin turnover in the lamellipodium occurs through *de novo* actin polymerization at the lamellipodial tip with retrograde flow away from the leading edge and in stress fibers through the incorporation of new actin monomers or filaments. Stress fibers were bleached away from focal adhesions. Thus, actin turnover inside the filaments is expected to result from incorporation of unbleached actin from the cytoplasmic pool. In the lamellipodium, a ROI for analysis was selected at the lamellipodium tip inside the photobleached region following the retrograde flow of *de novo* polymerization below the plasma membrane. Raw data were fitted with simFRAP plugin in ImageJ. For each acquisition reference cell, photobleached cell and bleached area are selected to extract the mobile fraction F_m. Data were plotted and analyzed in Prism version 6 (GraphPad software).

Antibodies and western blotting

Primary antibodies used were polyclonal rabbit anti-Septin 7 (IBL, #18991), and monoclonal mouse anti-β-actin (Sigma-Aldrich, #A5316), anti-CDC42 (BD Transduction Laboratories, #610929), anti-RAC1 (Abcam, Cat# ab33186) as well as anti-ArpC3 p21-Arc (Clone26, #612234, BD Transduction Laboratories). Secondary antibodies were anti-mouse (Bio-Rad, #170-6516) and anti-rabbit (Bio-Rad, #170-6515) horseradish peroxidase-conjugated. To quantify knockdown efficiency by immunoblotting, siRNA treated HeLa cells were lysed with RIPA buffer containing protease inhibitor (Roche, #11836170001) for 30 min at 4°C. Protein quantification of lysates was done with the Micro BCA™ Protein Assay Kit (Thermo Fisher Scientific, #23235) and 10 μg of total protein was loaded into NuPAGE 4%–12% Bis-Tris Protein Gels (Thermo Fisher Scientific, #NP0321BOX) or 12% SDS-PAGE gels. Proteins were transferred to a nitrocellulose membrane using the Trans-Blot® Turbo RTA Mini Nitrocellulose Transfer Kit (Bio-Rad, #1704270) and Trans-Blot© Turbo Transfer System (Bio-Rad, #1704150) or tank blotting system in Towbin Buffer (Tris 25 mM, Glycine 190 mM, 20% Methanol pH 8.3) during 1h at 300 mA at 4°C. Antibody detection was carried out with the SuperSignal West Pico PLUS Chemiluminescent Substrate (Thermo Fischer Scientific, #34577) with actin as loading control.

QUANTIFICATION AND STATISTICAL ANALYSIS

Time lapse microscopy series were analyzed using Icy (http://icy.bioimageanalysis.org/), Volocity 6.3 (PerkinElmer), or Fiji (http://fiji.sc) to determine starting points of foci formation, actin cocoon assembly, actin cocoon lifetime, vacuolar rupture time, and localization of host proteins. At least three biologically independent experiments per condition were performed. Quantitative data are mean values with error bars indicating ± Standard Deviation (SD) if not mentioned differently. Statistical analysis was performed in GraphPad Prism version 6. If not indicated differently, statistical significance was determined using a two-tailed Student's t test (Mann-Whitney) or a one-way ANOVA followed by Dunnett's multiple comparison test. (ns) not significant, $p < 0.05$ was considered as significant: *$p < 0.05$, **$p < 0.01$, ***$p < 0.001$, ****$p < 0.0001$.

Quantitative image analysis

Since almost all invading wild-type *Shigella* escaped into the host cytoplasm in the duration of the experiment, we focused in our analysis on *Shigella* that successfully invaded the cytosol (galectin-3 recruitment to BCV membrane remnant) as indicator for efficient infection. Time-lapse of *Shigella* WT infecting HeLa cells co-expressing actin-GFP and galectin-3-mOrange allowed correlation and precise timing of actin dynamics with vacuolar rupture. Actin cocoon assembly was defined as the *de novo* formation of an actin-enriched structure around the BCV membrane with clear borders that assembled *de novo* after cellular entry and before vacuolar rupture for a duration of > 2 min. The comparison of the overall percentage of bacteria that assemble an actin cocoon before vacuolar rupture did represent a solid readout to investigate e.g., the effect of host protein inhibitors or *Shigella* mutant strains. Cases in which cocoons could not be clearly distinguished from surrounding membrane ruffles or IAMs were excluded from analysis (0%–2% per experiment, within the error range). The presence or absence of actin cocoons was investigated. Changes in dynamics, shape, or relative fluorescence intensities were not taken into account. This study focused on primary infections and early invasion steps. Secondary infections usually lack the massive membrane ruffling of primary infections and were not taken into account.

The vacuolar rupture time was used as supporting readout and was defined as time span between the onset of initial membrane ruffling and the first appearance of galectin-3 recruitment to the BCV membrane remnant. This includes the successive (actin-dependent) invasion steps of cellular uptake, actin cocoon formation, cocoon maintenance as well as its disassembly, and cytosolic escape of *Shigella* (Figure S1D). Since other endocytic compartments than the BCV (e.g., *E. coli* InvA phagosomes, IAMs) were never galectin-3-positive, its recruitment was used as marker for *Shigella* entering the cytosol. All rupture events were considered including statistic outliers. Significance was likewise confirmed for the geometrical mean and datasets excluding statistical outliers. In screens with varying infection efficiencies (e.g., *Shigella* mutants), only the first invader per cell was taken into account.

To compare the actin cocoon with cellular or pathogen-induced actin structures (Figure 2A), we normalized the effect of extensive membrane ruffling at the bacterial entry site and of varying actin-GFP expression levels in different cells. We measured

the fluorescence intensity of on average the 10 most intense cellular actin stress fibers (mainly ventral and dorsal stress fibers, not in close proximity to focal adhesions) of each infected HeLa cell. The average stress fiber intensity was used to normalize the fluorescence intensity of each individual actin structure measurement per cell. In addition, each single measurement was corrected for the cytosolic actin-GFP signal in its immediate vicinity. *E. coli* InvA is a model for canonical phagocytosis with actin assembly and disassembly cycles around phagosomes (actin flashing). The related enteropathogenic *Salmonella* (*S.* Typhimurium) injects some T3SS effector protein homologs to *Shigella*. Data obtained for *E. coli* InvA and *Salmonella* infections were analyzed equally. The maximum intensity of actin assembly was considered. The lifetime of actin coats around *Shigella*'s BCV or *E. coli*'s phagosome (Figure 2C) was measured as the time interval between initial actin assembly and its complete disassembly. For *E. coli* InvA phagosomes, one cycle of complete actin assembly and disassembly was considered.

To quantify and correlate the PI3P peak with either the actin cocoon at *Shigella*'s BCV or actin flashing at phagosomes, we monitored over time the recruitment of the fluorescently labeled PI3P probe 2xFYVE and actin to the corresponding endocytic compartments (Figures 2E–2H). Each single measurement was corrected for the cytosolic background signal in its immediate vicinity. Data were normalized by dividing the fluorescence intensities of each 2xFYVE and actin time point by the respective maximum intensity. Individual experiments were aligned to the time point of maximum relative fluorescence intensity of the short-lasting 2xFYVE peak for *Shigella*, and the short-lasting actin peak for *E. coli* InvA. The variation of the actin signal at later time points for *Shigella* (Figure 2F) illustrates differences in actin cocoon dynamics.

All siRNA experiments were performed in parallel with scramble siRNA controls and HeLa cell controls. Septin 7 is an essential septin filament component and its knockdown by RNA interference efficiently inhibits septin filament assembly (Sirianni et al., 2016). Knockdown of ArpC3 was shown previously to be involved in *Shigella* invasion (Mellouk et al., 2014). For CDC42 siRNA-mediated knockdown or overexpression of CDC42 mutants, in parallel to the total population we also analyzed the behavior of only the first invading bacterium per cell (Figures S5D and S5E). Both analyses gave consistent results. Successful knockdown of CDC42 and ARPC3 by siRNA was also visible by altered actin cytoskeleton rearrangements at entry sites.

The intensity of host protein recruitment (Figures 5C–5G, 6, and S7) was quantified using Fiji. To investigate levels of CDC42 (UniProt# P60953-1) recruitment during *Shigella* infection, the mean fluorescence intensity of a ROI comprising either only the plasma membrane ruffle that formed the endocytic compartment, or the BCV membrane was measured (Figure 5D). All values were normalized to the initial signal of plasma membrane-recruited CDC42 to measure changes of CDC42 localization at the BCV in successive infection steps. We also analyzed the IcsB-dependent localization of CDC42 and N-WASP around vacuolar *Shigella* (Figures 6F, 7D, and 7F). Both proteins were considered constantly localized if they, after initial recruitment during early infection steps, remained associated with the galectin-3-stained membrane remnant after vacuolar rupture. This indicated that both proteins localized at BCV membrane remnants after rupture, but we observed different recycling behaviors for example for N-WASP and galectin-3. Proteins were defined as depleted in case they were initially recruited to the intact BCV, but disappeared before vacuolar rupture. CDC42 and N-WASP were specified as not recruited, if no localization at the vacuolar membrane was observed after scission of newly formed phagosomes. This does not exclude e.g., initial CDC42 recruitment to the plasma membrane during membrane ruffling. We considered only bacteria that successfully entered the host cytosol as indicated by galectin-3 (Gal-3) recruitment.

To analyze how actin cocoon assembly affects the fate of individual bacteria after vacuolar rupture, we quantified time lapses from HeLa cells co-expressing actin and galectin-3. The cytosolic fluorescence background from labeled proteins, marker recruitment to the bacterium during successive infection steps, and the characteristic shape of *Shigella* (individual actin tail, spreading behavior, replication state and size) is sufficient to track single bacteria inside the cell. We followed the infections steps of individual bacteria for 2 hr and monitored the time point of rupture, start and stopped movement, the kind of motility, the kind of vacuolar membrane recycling, and the fate of the bacteria after 2 hr infection. As 'protrusion', we defined actin tail-driven membrane protrusion for cell-to-cell spread and as 'motile' the intracellular movement by actin tail. Bacteria were defined as 'trapped', if after initial spreading they stopped movement, actin tail formation and growth for replication (or few cases that were never motile after rupture). With regard to the fate of the vacuolar membrane remnant, we defined 'quick recycling' if the membrane was quickly recycled away from a not yet moving bacterium. 'Sticky' defined cases where the bacterium lost the membrane remnant mainly by moving away from it and leaving it behind. As membrane 'cap' were all cases classified where bacteria remain surrounded by a part of the BCV during the entire infection. In most cases, bacteria were surrounded by half of the vacuolar membrane, which allowed moving with the cap by actin tail through the cytosol, but in some cases the ruptured BCV surrounded the bacteria completely.

Cell Reports, Volume *31*

Supplemental Information

Actin Assembly around the *Shigella*-Containing Vacuole Promotes Successful Infection

Sonja Kühn, John Bergqvist, Magdalena Gil, Camila Valenzuela, Laura Barrio, Stéphanie Lebreton, Chiara Zurzolo, and Jost Enninga

Inventory of Supplemental Information

SUPPLEMENTAL FIGURES

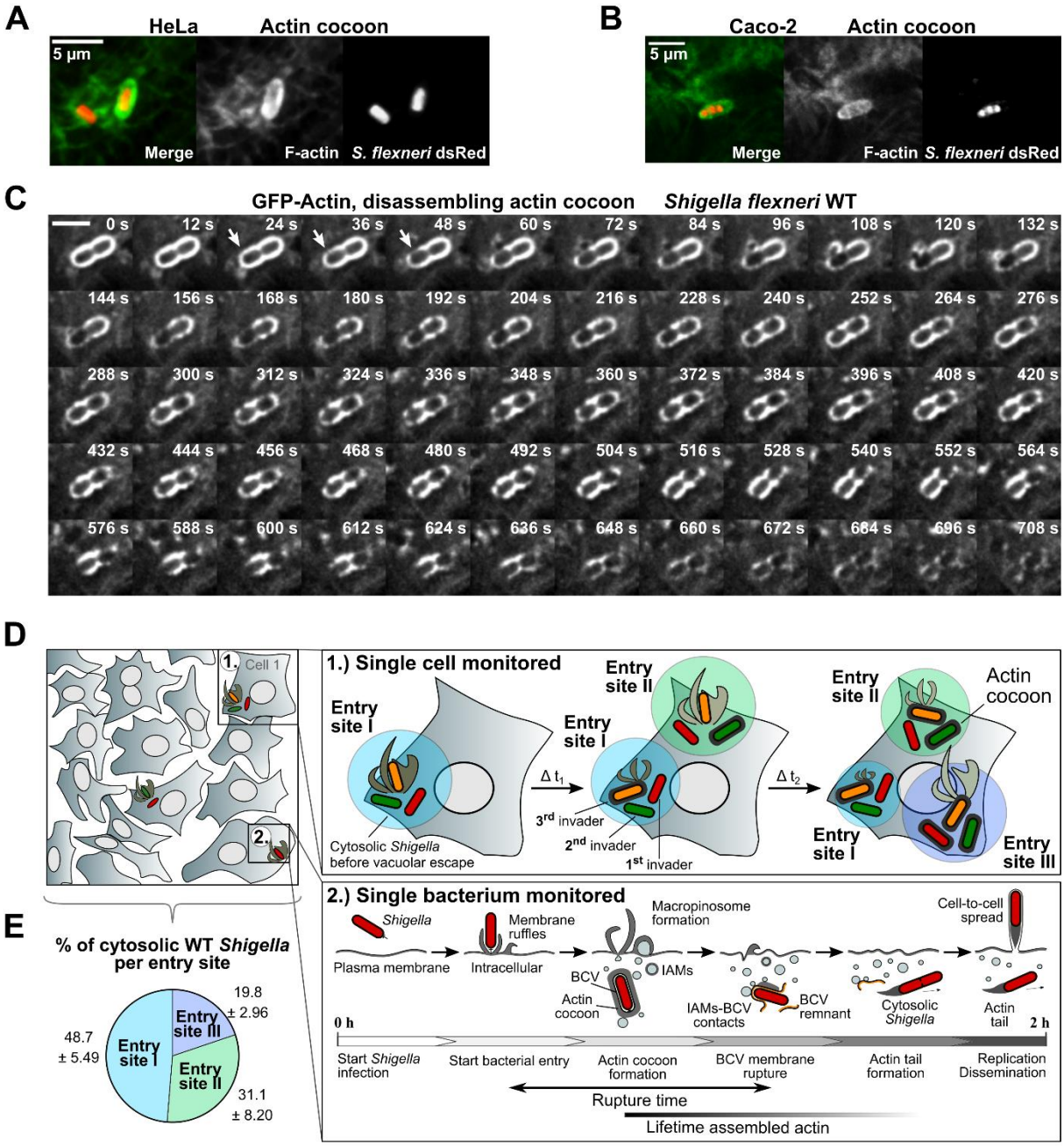

Figure S1. Actin cocoons contain F-actin and their formation depends on the order of infection, Related to Figure 1

(**A-B**) Immunofluorescence images of HeLa (A) and Caco-2 cells (B) expressing endogenous actin. Cells were infected with DsRed-expressing *Shigella* WT strain and phalloidin-labeled for F-actin (green). (**C**) Real-time images showing that actin cocoons disassemble simultaneously at different locations while undergoing constant reassembly during *Shigella* WT infection in actin-GFP expressing HeLa cells (scale bar: 3 μm). (**D**) Experimental setup to investigate successive invasion steps of *Shigella* in real time. Successive steps are monitored simultaneously at single cell (1) and single bacterium (2) levels. This allows correlating them within the cellular context and with other invading bacteria. In this setup (at MOI of 40; Figure S2), single cells were infected on average via three (3.03±0.46) distinct entry sites per cell (I, II, and III). The 1^{st} (red), 2^{nd} (green) and 3^{rd} (orange) invader of each entry site were considered in our analysis. (**E**) Almost half of the cytosolic *Shigella* WT entered host cells via the 1^{st} entry site, while about 1/3 bacteria invaded via the 2^{nd} and 1/5 via the 3^{rd} foci. (**F-G**) Rupture time (F) and actin cocoon assembly (G) depend on the entry site and order of infection. Depicted is the in-depth analysis of *Shigella* WT that developed an actin cocoon from Figure 1F, G (n=4, N=446). The rupture time of individual 1^{st}, 2^{nd}, or 3^{rd} bacteria invading the same cell through different entry sites is similar (F). The probability of actin cocoon formation for individual bacteria depends on the order of infection and the specific entry site (G). All late invading bacteria polymerize an actin cocoon. All 3^{rd} invaders of foci II and III in all independent experiments had an actin cocoon. Error bars indicate ± SD (F), Mann-Whitney test with $p<0.05$ as significant (*$p<0.05$, ns: not significant). In (E, G), mean values ± SD are indicated.

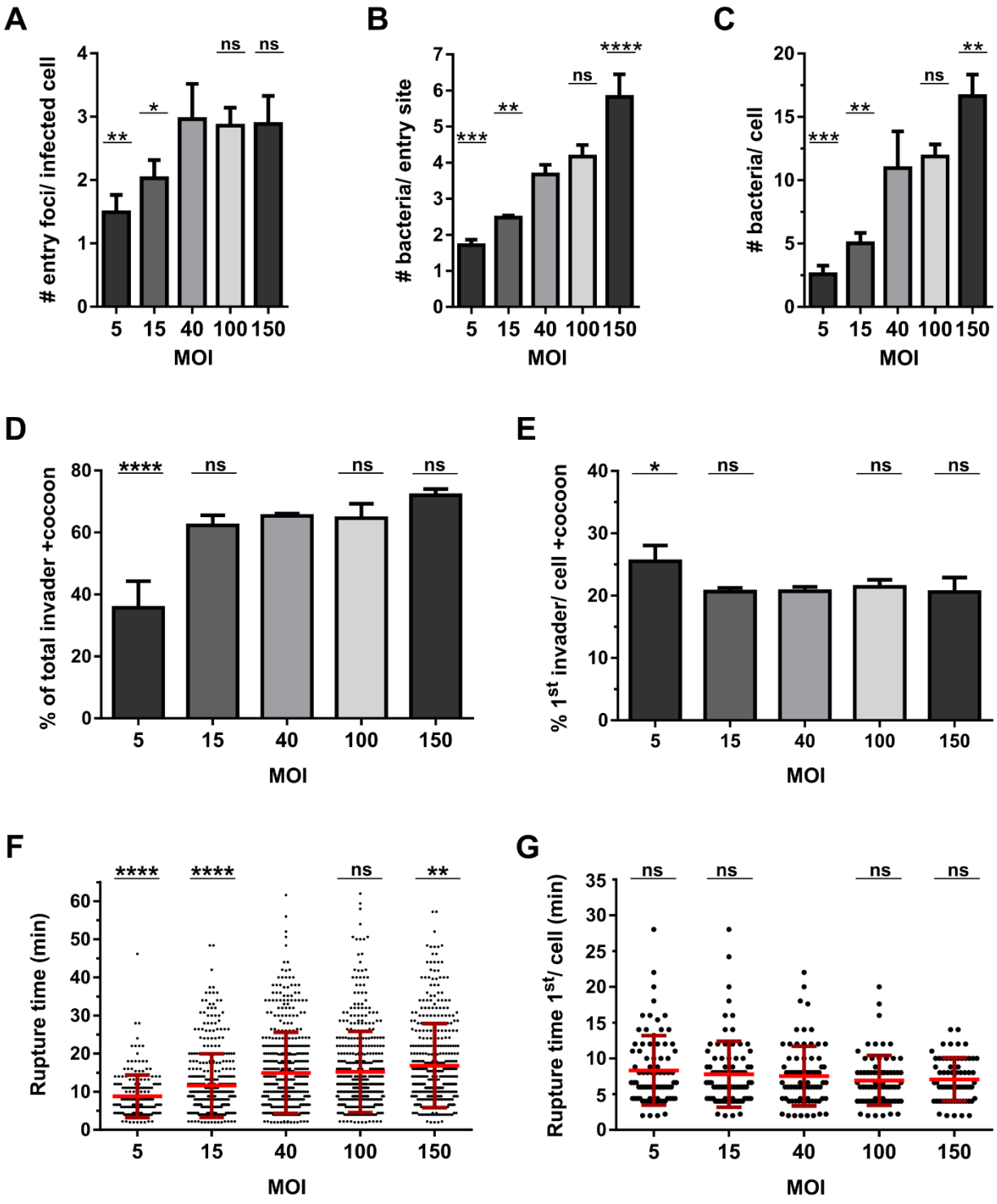
A
entry foci/ infected cell
**
*
ns
ns
MOI
5
15
40
100
150
B
bacteria/ entry site
***
**
ns
****
C
bacteria/ cell
***
**
ns
**
D
% of total invader +cocoon
****
ns
E
% 1st invader/ cell +cocoon
*
F
Rupture time (min)
****
****
ns
**
G
Rupture time 1st/ cell (min)

Figure S2. The multiplicity of infection (MOI) defines the number of entering *Shigella* per individual cell, but not the probability of actin cocoon formation, Related to Figure 1

The effect of MOIs from 5 to 150 was investigated with regards to entry sites per infected cell (**A**), successfully invading bacteria per entry site (**B**), overall number of invading bacteria per cell (**C**), the probability of cocoon formation (**D-E**) and vacuolar escape time (**F-G**). The higher the MOI, the more bacteria enter via the same entry site. The quickly saturated effect of the MOI to cocoon formation (D) and rupture time (F) is likely caused by the increased probability for cocoon assembly of later entering bacteria (Figure S1). Since with high MOI more bacteria per entry site invade host cells, there are more late invaders present that assemble an actin cocoon. This probably increases the percentage of the total cytosolic *Shigella* with cocoons at higher MOIs compared to very low ones. Comparing the same bacterial population, here the 1st invading *Shigella* per cell, leads to no difference in actin cocoon formation and vacuolar escape (E, G). In (A-D, F), total invading *Shigella* populations were analyzed (n=3, N=2000 bacteria with MOI 5: 203, MOI 15: 430, MOI 40: 477, MOI 100: 461, MOI 150: 429)). In (E, G), only the 1st invaders per cell of the same experiments were taken into account (N=385 with MOI 5: 81, MOI 15: 86, MOI 40: 78, MOI 100: 72, MOI 150: 68). Mean values ± SD are indicated as error bars. Statistical significance was determined using one-way ANOVA or Student's *t*-test comparing individual MOI experiments with MOI 40. $p<0.05$ was considered as significant (*$p<0.05$, **$p<0.01$, ***$p<0.001$, ****$p<0.0001$, ns: not significant).

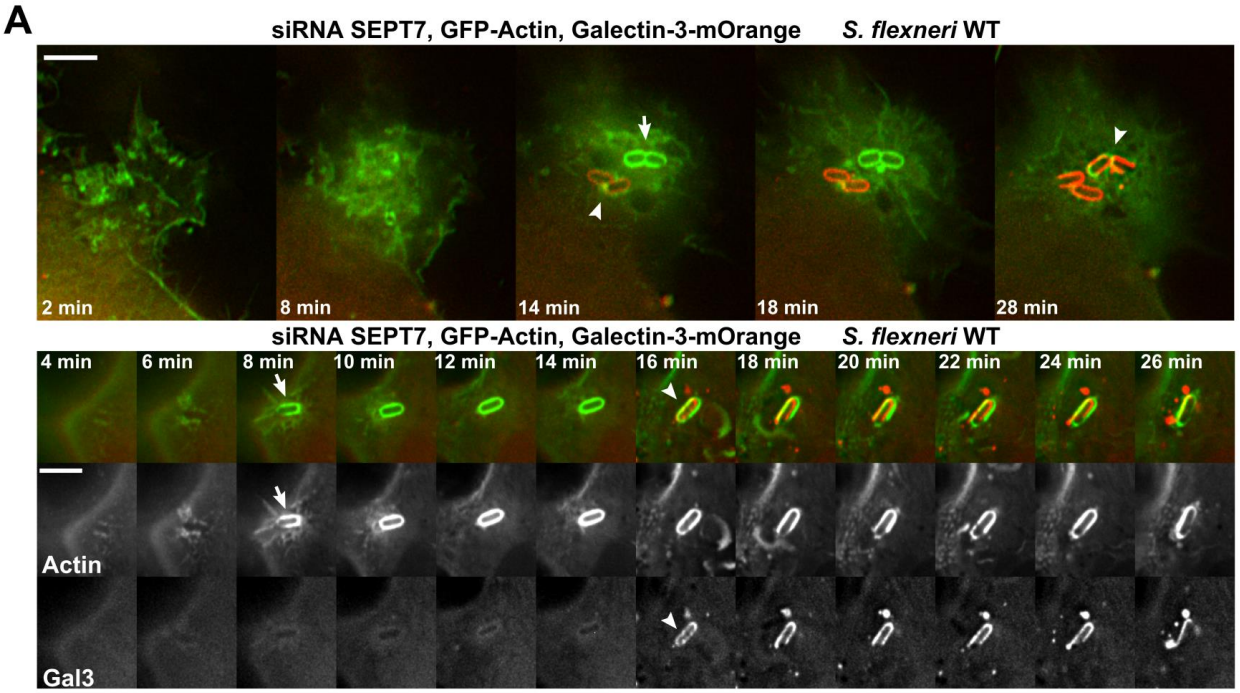
A
siRNA SEPT7, GFP-Actin, Galectin-3-mOrange
S. flexneri WT
2 min
8 min
14 min
18 min
28 min
siRNA SEPT7, GFP-Actin, Galectin-3-mOrange
S. flexneri WT
4 min
6 min
8 min
10 min
12 min
14 min
16 min
18 min
20 min
22 min
24 min
26 min
Actin
Gal3

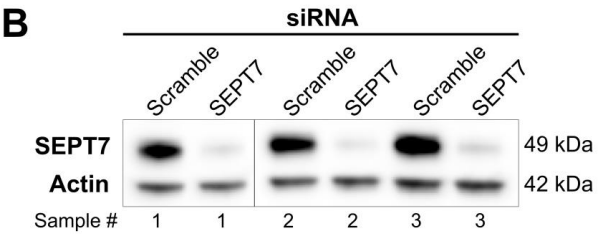
B
siRNA
Scramble
SEPT7
SEPT7
Actin
49 kDa
42 kDa
Sample #
1 1 2 2 3 3

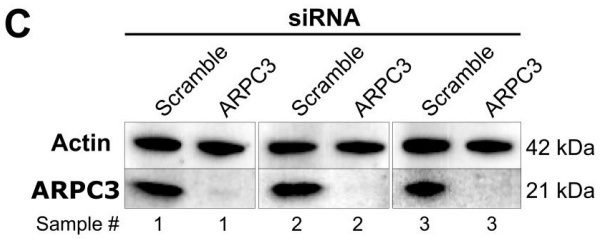
C
siRNA
Scramble
ARPC3
Actin
ARPC3
42 kDa
21 kDa
Sample #
1 1 2 2 3 3

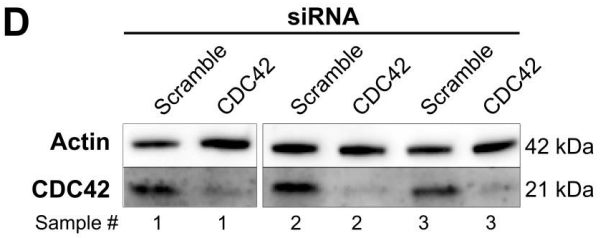
D
siRNA
Scramble
CDC42
Actin
CDC42
42 kDa
21 kDa
Sample #
1 1 2 2 3 3

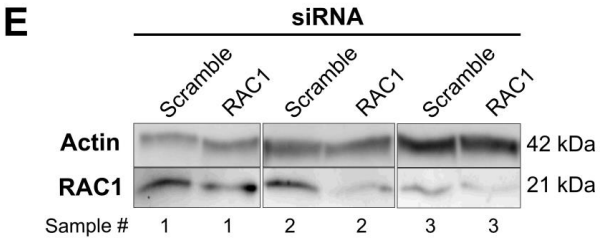
E
siRNA
Scramble
RAC1
Actin
RAC1
42 kDa
21 kDa
Sample #
1 1 2 2 3 3

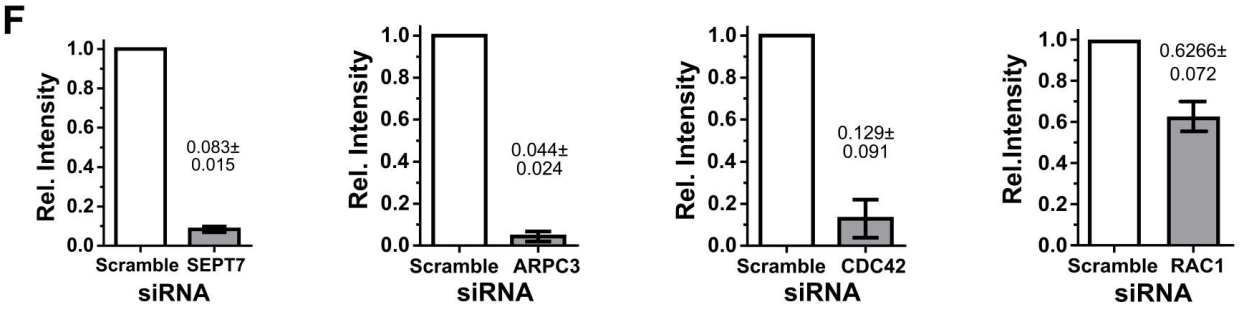
F
Rel. Intensity
0.083± 0.015
Scramble SEPT7
siRNA
0.044± 0.024
Scramble ARPC3
siRNA
0.129± 0.091
Scramble CDC42
siRNA
0.6266± 0.072
Scramble RAC1
siRNA

Figure S3. Characterization of the actin cocoon and the tools for its analysis, Related to Figure 2, 4 and 6

(**A**) Septin 7 knockdown does not prevent actin cocoon assembly. Representative time-lapses of HeLa cells treated with SEPTIN 7 (SEPT7) siRNA and co-transfected with actin and galectin-3. Upper panel: entry site during *Shigella* WT infection, lower panel: actin cocoon dynamics and successive infection steps during invasion of an individual *Shigella* bacterium. t=0 min: start entry site formation, arrow: start cocoon assembly, arrow head: BCV rupture, scale bar: 5 µm. (**B-E**) Western blot validation of siRNA treatments against SEPT7 (B), the Arp2/3 complex component ARPC3 (C), CDC42 (D) and RAC1 (E). Samples of n=3 independent experiments are shown compared to scramble siRNA control. (**F**) Quantification of unmodified images revealed knockdown (KD) efficiencies of 91.7% (SEPT7, A), 95.6% (ARPC3, B), 87.1% (CDC42, C) and 37,3% (RAC1, D). Of note, CDC42 knockdown, although less efficient, had a stronger effect on cocoon assembly than ARPC3 knockdown. This could indicate other CDC42 functions in cocoon formation beside Arp2/3 complex activation. The contrast in the figures was enhanced to highlight KD efficiency.

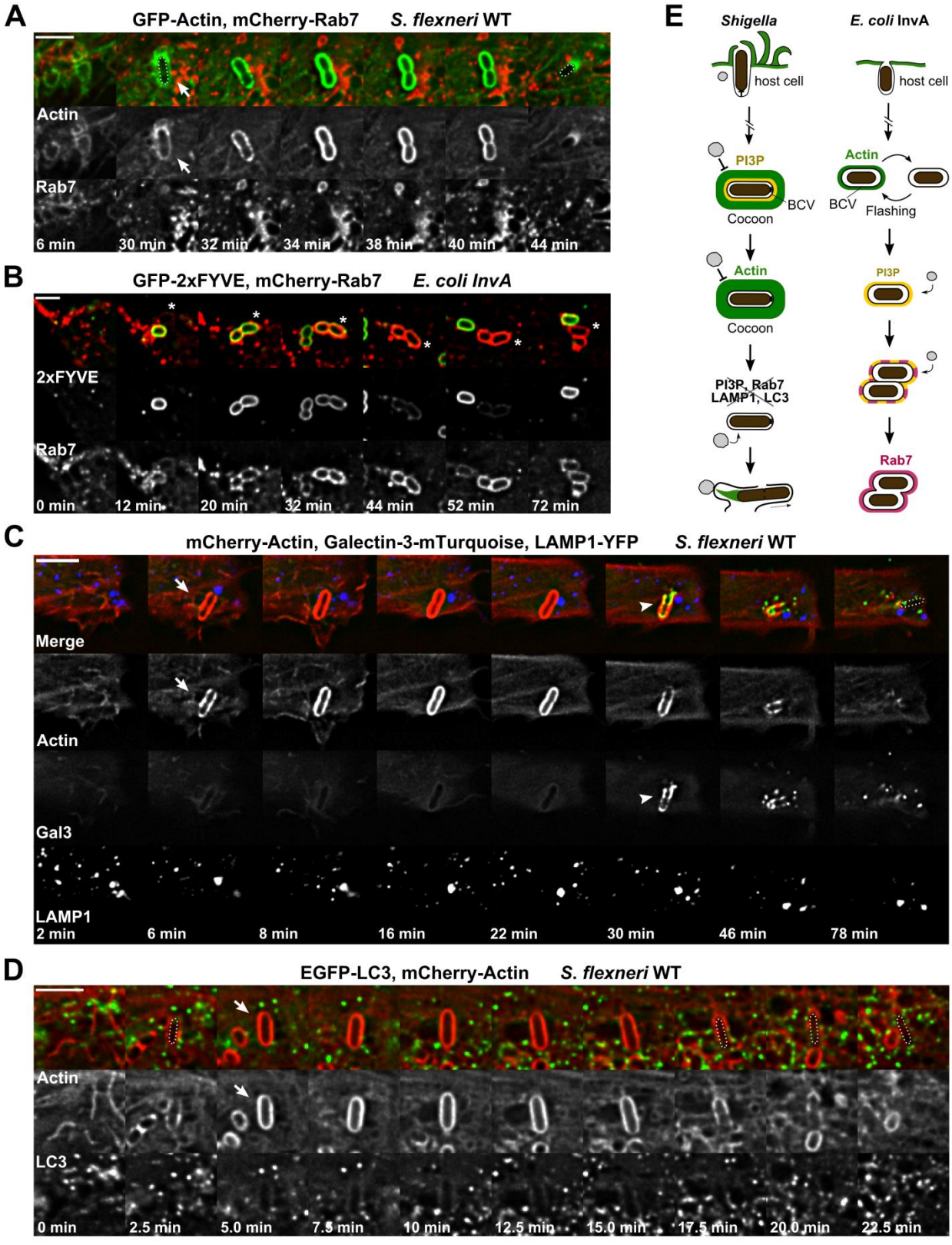
A
GFP-Actin, mCherry-Rab7
S. flexneri WT
Actin
Rab7
6 min
30 min
32 min
34 min
38 min
40 min
44 min
B
GFP-2xFYVE, mCherry-Rab7
E. coli InvA
2xFYVE
Rab7
0 min
12 min
20 min
32 min
44 min
52 min
72 min
E
Shigella
E. coli InvA
host cell
host cell
PI3P
BCV
Cocoon
Actin
BCV
Flashing
Actin
Cocoon
PI3P
PI3P, Rab7
LAMP1, LC3
Rab7
C
mCherry-Actin, Galectin-3-mTurquoise, LAMP1-YFP
S. flexneri WT
Merge
Actin
Gal3
LAMP1
2 min
6 min
8 min
16 min
22 min
30 min
46 min
78 min
D
EGFP-LC3, mCherry-Actin
S. flexneri WT
Actin
LC3
0 min
2.5 min
5.0 min
7.5 min
10 min
12.5 min
15.0 min
17.5 min
20.0 min
22.5 min

Figure S4. Markers for canonical endosomal maturation and autophagy are not recruited to the *Shigella* BCV surrounded by the actin cocoon, Related to Figure 2

(**A**) Representative time-lapse monitoring Rab7 localization during *Shigella* WT infection. (**B**) Time-lapse imaging showing the maturation of *E. coli* InvA phagosomes and recruitment of Rab7 after the initial PI3P peak. (**C-D**) Time-lapse imaging of LAMP1 (C) and LC3 (D) localization during *Shigella* WT infection indicates no recruitment to the BCV. For *Shigella*, HeLa cells were co-transfected with the corresponding fluorescent marker protein and actin to monitor the successive infection steps from membrane ruffle to actin tail formation. All bacteria were moving inside the cell in the last shown image, indicating cytosolic bacteria that successfully escaped the BCV. t=0 min: start entry site formation, arrow: start cocoon assembly, arrow head: BCV membrane rupture indicated by galectin-3 recruitment, scale bars: 5 μm (A, C-D), 3 μm (B). Selected *Shigella* WT and *E. coli InvA* bacteria are highlighted with dashed lines and stars, respectively. (**E**) Model illustrating the localization of autophagy and maturation markers at the *Shigella* BCV and the *E. coli* InvA phagosome. The *Shigella* BCV exhibits an altered maturation process after rapid depletion of PI3P leading to rupture with intracellular replication and dissemination. This is different to canonical phagosomes: After actin flashing, the phagosome becomes PI3P positive followed by Rab7 recruitment and PI3P depletion for vesicle fusion events with vacuolar maturation and degradation.

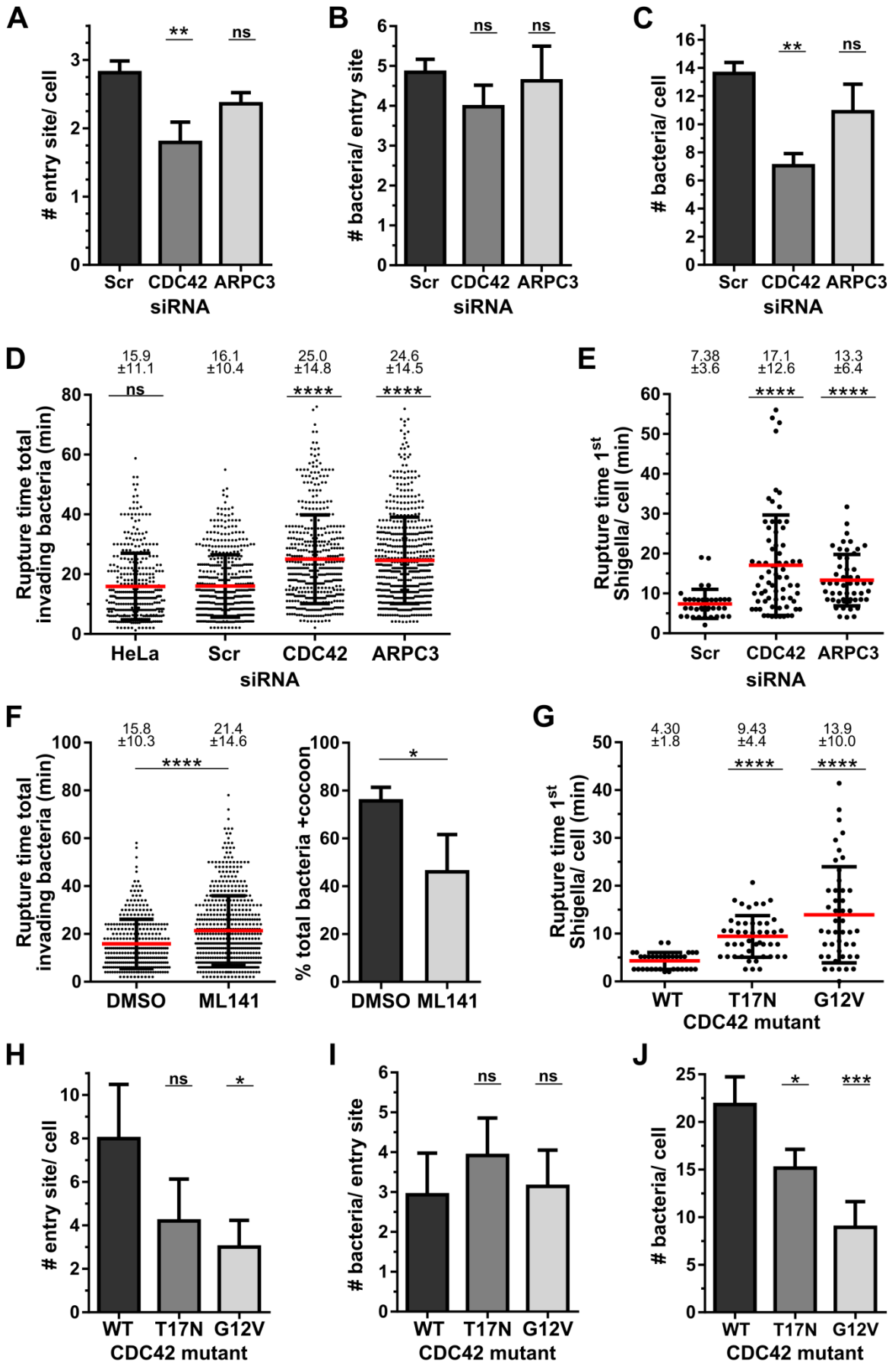
A
entry site/ cell
**
ns
Scr
CDC42
ARPC3
siRNA
B
bacteria/ entry site
ns
ns
Scr
CDC42
ARPC3
siRNA
C
bacteria/ cell
**
ns
Scr
CDC42
ARPC3
siRNA
D
15.9 ±11.1
16.1 ±10.4
25.0 ±14.8
24.6 ±14.5
ns
****
****
Rupture time total invading bacteria (min)
HeLa
Scr
CDC42
ARPC3
siRNA
E
7.38 ±3.6
17.1 ±12.6
13.3 ±6.4
****
****
Rupture time 1st Shigella/ cell (min)
Scr
CDC42
ARPC3
siRNA
F
15.8 ±10.3
21.4 ±14.6
****
Rupture time total invading bacteria (min)
DMSO
ML141
*
% total bacteria +cocoon
DMSO
ML141
G
4.30 ±1.8
9.43 ±4.4
13.9 ±10.0
****
****
Rupture time 1st Shigella/ cell (min)
WT
T17N
G12V
CDC42 mutant
H
ns
*
entry site/ cell
WT
T17N
G12V
CDC42 mutant
I
ns
ns
bacteria/ entry site
WT
T17N
G12V
CDC42 mutant
J
*
***
bacteria/ cell
WT
T17N
G12V
CDC42 mutant

Figure S5. CDC42 and the Arp2/3 complex are involved in host cell invasion, Related to Figure 4
Depicted are additional statistics for the experiments shown in Figure 4. Only bacteria that successfully escaped into the host cytosol were considered for quantitative analysis. (**A-E**) Knockdown of CDC42 and ARPC3. Decreased cellular levels of CDC42 lowered the number of entry sites per infected cell (A) and thus the number of invading bacteria per cell (C). Decreased levels of CDC42 and ARPC3 delayed the rupture times for all invading bacteria per experiment (D) and the first invaders per cell (E). Knockdown efficiency was confirmed by immunoblotting (Figure S3). (**F**) Inhibition of CDC42 with the inhibitor ML141 increases the rupture time (left) and impairs cocoon assembly (right) around vacuolar *Shigella*. (**G-J**) HeLa cells co-expressing galectin-3 and CDC42 WT, T17N or G12V were infected with *Shigella* WT. Presented are the rupture time of the first invading *Shigella* per cell (G), number of entry sites per cell (H), number of bacteria per entry site (I), and total number of invading bacteria per cell (J). Depicted are error bars indicating ± SD, or mean values ± SD. One-way ANOVA or Student's *t*-test was used to determine significance compared to infected Scr or DMSO control or to CDC42 WT-expressing cells. $p<0.05$ was considered as significant (*$p<0.05$, **$p<0.01$, ***$p<0.001$, ****$p<0.0001$, ns: not significant). Counted events: (A-D) no siRNA (HeLa): N=374, control scramble siRNA (Scr): N=481, siRNA CDC42: N=464, siRNA ARPC3: N=573; (E) Scr siRNA: N=36, siRNA CDC42: N=69, siRNA ARPC3: N=52; (F) DMSO (control): N=341, ML141: N=553; (G): WT: N=34, T17N: N=47, G12V: N=47; (H-J): WT: N=373, N=T17N: N=375, G12V: N=375.

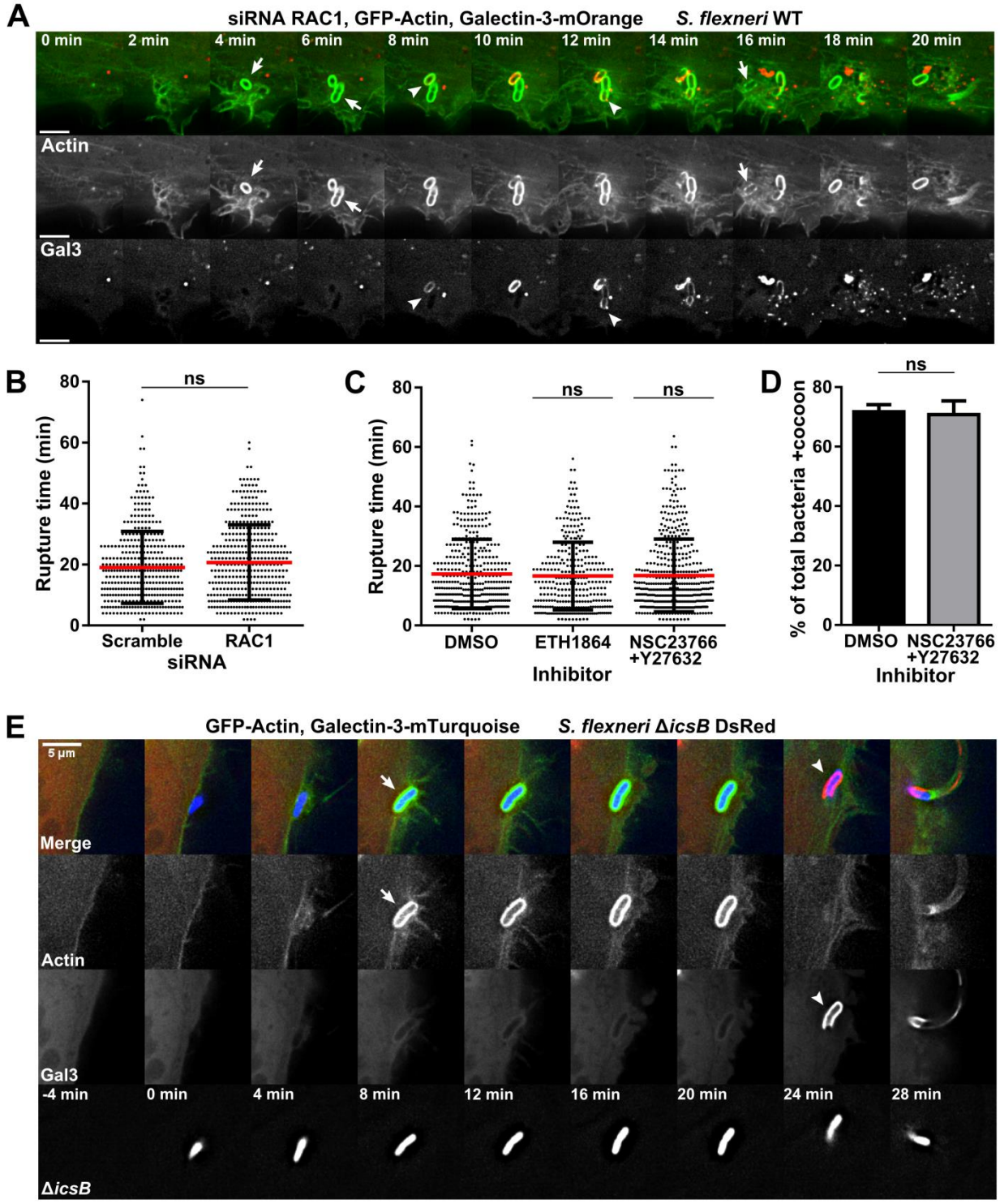
A
siRNA RAC1, GFP-Actin, Galectin-3-mOrange
S. flexneri WT
0 min
2 min
4 min
6 min
8 min
10 min
12 min
14 min
16 min
18 min
20 min
Actin
Gal3
B
Rupture time (min)
ns
Scramble
RAC1
siRNA
C
Rupture time (min)
ns
ns
DMSO
ETH1864
NSC23766 +Y27632
Inhibitor
D
% of total bacteria +cocoon
ns
DMSO
NSC23766 +Y27632
Inhibitor
E
GFP-Actin, Galectin-3-mTurquoise
S. flexneri ΔicsB DsRed
5 µm
Merge
Actin
Gal3
-4 min
0 min
4 min
8 min
12 min
16 min
20 min
24 min
28 min
ΔicsB

Figure S6. RAC1 is not required for actin cocoon assembly, Related to Figure 4 and 5

(**A-B**) Representative time-lapse (A) and quantification (B) of the experiment shown in Figure 4F. RAC1 knockdown does neither prevent actin cocoon assembly, nor affect the rupture time of invading *Shigella* WT. RAC1 siRNA treated HeLa cells were co-transfected with actin and galectin-3. (**C-D**) Small molecule inhibition of RAC1 (ETH1864, NSC23766) and ROCK (Y27632) did not interfere with the rupture time (C) or cocoon assembly (D). Error bars ± SD or mean values ± SD are illustrated, ns: not significant. Counted events: (B) scramble siRNA: N=386, siRNA RAC1: N=409; (C-D) DMSO: N=385, ETH1864: N=328, NCS23766+Y21632: N=464. (**E**) Representative time-lapse of HeLa cells co-transfected with actin and galectin-3 and infected with DsRed-expressing *Shigella* Δ*icsB*. t=0 min: start entry site formation, arrow: start cocoon assembly, arrow head: BCV membrane rupture, scale bars: 5 μm.

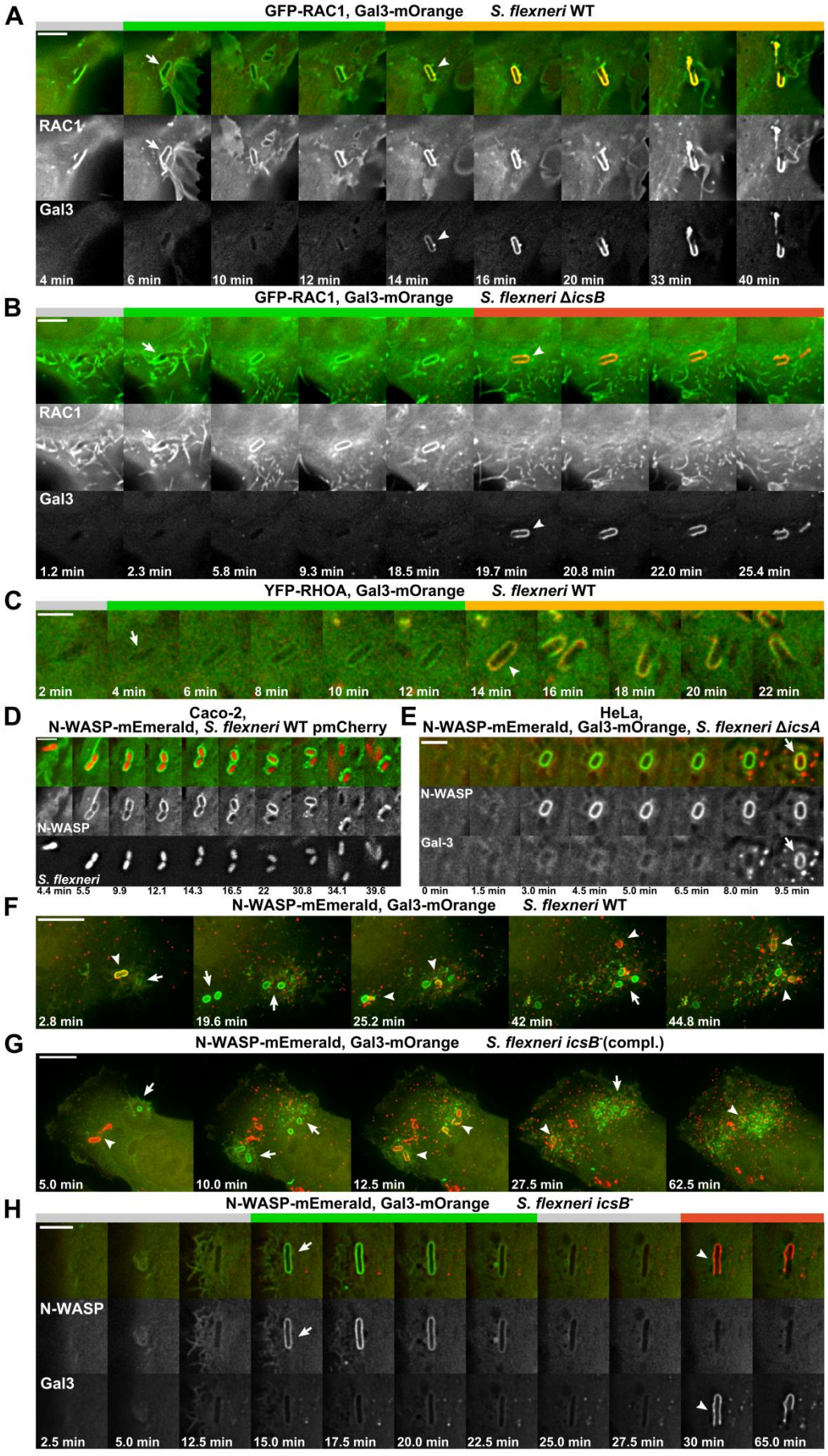
A
GFP-RAC1, Gal3-mOrange
S. flexneri WT
RAC1
Gal3
4 min
6 min
10 min
12 min
14 min
16 min
20 min
33 min
40 min
B
GFP-RAC1, Gal3-mOrange
S. flexneri ΔicsB
RAC1
Gal3
1.2 min
2.3 min
5.8 min
9.3 min
18.5 min
19.7 min
20.8 min
22.0 min
25.4 min
C
YFP-RHOA, Gal3-mOrange
S. flexneri WT
2 min
4 min
6 min
8 min
10 min
12 min
14 min
16 min
18 min
20 min
22 min
D
Caco-2,
N-WASP-mEmerald, S. flexneri WT pmCherry
N-WASP
S. flexneri
4.4 min 5.5
9.9
12.1
14.3
16.5
22
30.8
34.1
39.6
E
HeLa,
N-WASP-mEmerald, Gal3-mOrange, S. flexneri ΔicsA
N-WASP
Gal-3
0 min
1.5 min
3.0 min
4.5 min
5.0 min
6.5 min
8.0 min
9.5 min
F
N-WASP-mEmerald, Gal3-mOrange
S. flexneri WT
2.8 min
19.6 min
25.2 min
42 min
44.8 min
G
N-WASP-mEmerald, Gal3-mOrange
S. flexneri icsB-(compl.)
5.0 min
10.0 min
12.5 min
27.5 min
62.5 min
H
N-WASP-mEmerald, Gal3-mOrange
S. flexneri icsB-
N-WASP
Gal3
2.5 min
5.0 min
12.5 min
15.0 min
17.5 min
20.0 min
22.5 min
25.0 min
27.5 min
30 min
65.0 min

Figure S7. Rho GTPase and N-WASP recruitment to the BCV, Related to Figure 6

(**A-B**) RAC1 is recruited to most BCVs and localizes constantly around the *Shigella*-containing vacuole dependent on IcsB, like CDC42. Depicted are representative time-lapses of HeLa cells co-transfected with RAC1 and galectin-3 (Gal3) (scale bars: 5 μm). (**C**) Most bacteria do not recruit RHOA at their BCV. The time lapse shows an example of this occasional event in HeLa cells (22% of cytosolic bacteria; scale: 3 μm). (**D**) As in HeLa cells, N-WASP is likewise constantly localized around the BCV of mCherry-expressing *S. flexneri* WT (red) invading Caco-2 cells transiently expressing N-WASP (scale: 3 μm). (**E**) Constant N-WASP localization at the BCV is IcsA-independent. A representative time-lapse of HeLa cells co-transfected with N-WASP and galectin-3 and infected with *Shigella* Δ*icsA* is shown (scale: 3 μm). Initial N-WASP recruitment before vacuolar rupture and its constant localization are similar to WT infections (see Figure 6). (**F-H**) N-WASP is constantly localized at BCVs of WT (F) or IcsB-complemented *icsB*$^{-}$ (compl.) (G) strains (3.5 μm stacks of infection sites, scale bars: 10 μm). *Shigella icsB*$^{-}$ initially recruits N-WASP at its BCV, but does not cluster it there in the moment of vacuolar rupture (H, scale bar: 5 μm). *Shigella* strains in (F-H) were poly-L-lysine-coated. t=0 min: start entry, arrow: start cocoon, arrow head: BCV membrane rupture.